The structure of gravel-bed flow with intermediate submergence: A laboratory study

S. H. Mohajeri[1,2], S. Grizzi[3], M. Righetti[4], G. P. Romano[5], and V. Nikora[6]

[1]Department of Civil, Environmental and Mechanical Engineering, University of Trento, Trento, Italy, [2]School of Geography, Queen Mary, University of London, London, UK, [3]CNR—INSEAN, The Italian Ship Model Basin, Rome, Italy, [4]Faculty of Science and Technology, Free University of Bozen, Bozen, Italy, [5]Department of Mechanics and Aeronautics, University "LaSapienza," Roma, Italy, [6]School of Engineering, University of Aberdeen, Aberdeen, UK

Abstract The paper reports an experimental study of the flow structure over an immobile gravel bed in open channel at intermediate submergence, with particular focus on the near-bed region. The experiments consisted of velocity measurements using three-component (stereoscopic) Particle Image Velocimetry (PIV) in near-bed horizontal plane and two-component PIV in three vertical planes that covered three distinctly different hydraulic scenarios where the ratio of flow depth to roughness height (i.e., relative submergence) changes from 7.5 to 10.8. Detailed velocity measurements were supplemented with fine-scale bed elevation data obtained with a laser scanner. The data revealed longitudinal low-momentum and high-momentum "strips" in the time-averaged velocity field, likely induced by secondary currents. This depth-scale pattern was superimposed with particle-scale patches of flow heterogeneity induced by gravel particle protrusions. A similar picture emerged when considering second-order velocity moments. The interaction between the flow field and gravel-bed protrusions is assessed using cross correlations of velocity components and bed elevations in a horizontal plane just above gravel particle crests. The cross correlations suggest that upward and downward fluid motions are mainly associated with upstream-facing and lee sides of particles, respectively. Results also show that the relative submergence affects the turbulence intensity profiles for vertical velocity over the whole flow depth, while only a weak effect, limited to the near-bed region, is noticed for streamwise velocity component. The approximation of mean velocity profiles with a logarithmic formula reveals that log-profile parameters depend on relative submergence, highlighting inapplicability of a conventional "universal" logarithmic law for gravel-bed flows with intermediate submergence.

1. Introduction

Studies of rough-bed flows have intensified over recent decades reflecting significant demand for advanced information required by numerous engineering and environmental applications [e.g., *Raupach et al.*, 1991; *Nezu and Nakagawa*, 1993; *Finnigan*, 2000; *Jimenez*, 2004]. These studies include theoretical analyses, laboratory and field experiments, and numerical simulations. Both instantaneous and mean velocity fields have been studied with a wide use of various statistical methods and appropriately averaged hydrodynamic equations such as the Reynolds-Averaged Navier-Stokes (RANS) equations and/or double-averaged (in time and spatially within a thin slab parallel to the bed) equations [e.g., *Monin and Yaglom*, 1971; *Finnigan*, 2000; *Nikora et al.*, 2001; *Nikora et al.*, 2007a].

Concerning open-channel gravel-bed flows, *Nikora et al.* [2007b] identified four flow types depending on the relative submergence H_o/Δ, where $H_o = H + \Delta$, Δ is the roughness height and H is flow depth above the roughness crests. As shown in Figure 1, flow type I is flow of high relative submergence (e.g., $H_o/\Delta > 40{\sim}80$), flow type II is flow of intermediate relative submergence (e.g., $5 < H_o/\Delta < 40{\sim}80$), flow type III is low-submergence flow (e.g., $1 < H_o/\Delta < 5$), and flow type IV relates to partially inundated flow with $H_o/\Delta < 1$ [*Nikora*, 2008; *Nikora et al.*, 2007b]. The bounds of submergence H_o/Δ, shown above, are approximate and remain to be better justified. Although intermediate-submergence and low-submergence flows are common in nature, the knowledge on such flows remains limited in spite of the recent advances [e.g., *Buffin-Bélanger and Roy*, 1998; *Hardy et al.*, 2007, 2010]. A number of authors employed in their studies the double-averaging approach which is more appropriate for such flows compared to RANS. For example, *Manes et al.* [2007] concluded that the appropriately normalized flow statistics do not change with
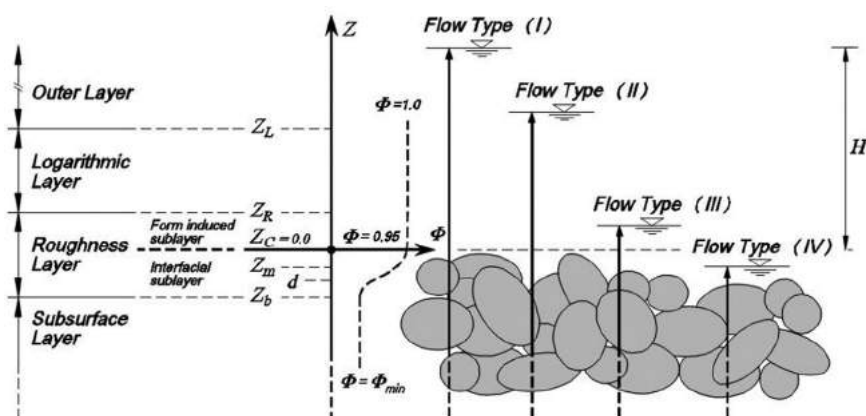
Figure 1. Subdivision of rough-bed open-channel flow into specific layers [*Nikora et al.*, 2001].

relative submergence except for the form-induced stresses. Form-induced stresses emerge as a result of spatial averaging, similar to the Reynolds stresses that appear as a result of time averaging [*Nikora et al.*, 2001]. In other words, they are correlation moments between deviations of the time-averaged velocities $\tilde{u}_i$ from their double-averaged counterparts $\langle \bar{u}_i \rangle$ (i.e., $\tilde{u}_i = \bar{u}_i - \langle \bar{u}_i \rangle$ and $u_i = \langle \bar{u}_i \rangle + \tilde{u}_i + u'_i$ where u_i is an ith component of the instantaneous velocity vector, overbar defines time averaging, square brackets define spatial averaging, and prime denotes a turbulent fluctuation). *Aberle et al.* [2008] found that form-induced stresses are negligible away from the bed but increase toward gravel particle crests. Recently, *Cooper et al.* [2013] studied the role of flow submergence on heterogeneity of the time-averaged flow due to the roughness elements by analyzing spatial variation of form-induced stresses. They showed that the effect of the relative submergence on the spatial velocity statistics is more noticeable for the streamwise velocity component than for the vertical velocity.

In the inner region of high-submergence rough-bed flow (flow type I), the distribution of the mean streamwise velocity is generally expected to follow the "universal" logarithmic law [e.g., *Jimenez*, 2004]. However, recent findings for smooth-bed turbulent flows question the idea of the "universality" of the log-law [e.g., *George*, 2007; *Smits et al.*, 2011; *Marusic et al.*, 2010], shedding doubts in relation to rough-bed flows too. Nevertheless, some data indicate that the logarithmic velocity distribution may be valid even for rough-bed flows with intermediate submergence (flow type II) although the von Kàrmàn constant κ, zero-plane displacement, and the log-law bounds have to be adjusted depending on the flow conditions and bed geometry [*Bayazit*, 1976; *Koll*, 2006; *Nikora*, 2008; *Gaudio et al.*, 2010]. The attempts to approximate measured velocity distributions with the logarithmic formula for flows with $H_o/\Delta < 40$ are numerous [e.g., *Nikora et al.*, 2002; *Koll*, 2006; *Manes et al.*, 2007; *Franca et al.*, 2008]. These studies show that with decrease in H_o/Δ, the deviations from the "universality" increase, i.e., the log-law parameters deviate from those obtained for flows with high relative submergence. Researchers have tried to account for these deviations by developing additional relationships linking the log-law parameters to roughness parameters and flow submergence H_o/Δ. The proposed relationships, however, are mostly empirical and reflect the trends that are likely flow-specific and thus may not be general (i.e., "universal").

Moreover, the results obtained by different authors are sometimes contradictory limiting possibilities for unambiguous interpretation of the correlation between the flow field features and bed characteristics. For example, *Buffin-Bélanger et al.* [2006] reported that distributions of the time-averaged velocity and turbulent kinetic energy in the near-bed region are not random but consistent with the local bed topography. These findings are partly in agreement with earlier experiments of *Lamarre and Roy* [2005]. According to *Lamarre and Roy* [2005], mean and turbulent flow characteristics are affected locally near roughness elements. At greater scale, they did not notice any strong dependence of turbulent flow characteristics on individual roughness elements. However, sampling spacings in both these studies were too coarse for assessment of the dependence of the flow organization on bed properties at the scale of individual roughness elements or at finer scales. At the same time, *McLean and Nikora* [2006] found noticeable correlation between form-induced velocity components $\tilde{u}_i$ and bed elevation variations caused by individual gravel particles. They

showed that the near-bed velocity distribution in a plane parallel to the bed exhibits quite a stable pattern. Vertical velocity usually attains maximum (positive) values above the upstream slopes of gravel particles and minimum (negative) values above their downstream slopes. The distribution of the streamwise velocity was different. Although it resembles, to a certain degree, the pattern of the vertical velocity, it is shifted downstream and is coherent, in a statistical sense, with bed elevations. *Cooper and Tait* [2008], however, did not observe significant correlation between near-bed flow and bed topography at a grain scale in a gravel-bed flow. Also, *Cooper and Tait* [2008] highlighted the presence of depth-scale alternating high and low time-averaged velocity "strips" near the bed, with widths depending on relative submergence. *Cooper and Tait* [2008] argued that the observed strips cannot be ascribed to secondary current cells, given the high aspect ratio B/H in their experiments (B is channel width). It is indeed generally accepted that secondary currents are significant in narrow channels where $B/H < 5$ [*Nezu and Nakagawa*, 1993]. However, in recent years the secondary currents have been also observed in rough-bed channels with much higher aspect ratios [*Nikora et al.*, 1998b; *Rodríguez and García*, 2008; *Albayrak and Lemmin*, 2011]. The data given in *Cooper and Tait* [2008] are consistent with secondary currents signatures (e.g., "strip" spacing, dependence on relative submergence) and therefore the phenomenon discovered by *Cooper and Tait* [2008] may in principle relate to the cellular secondary currents.

The studies highlighted above show that there is still a lack of systematic information on gravel-bed flows at intermediate relative submergence. The relations between bed topography, mean flow, and turbulence characteristics in near-bed region are not lucid although some notable features have been reported. Also, it is not clear how the effects of bed topography and secondary currents mix together at different relative submergence. To address these issues, a series of experiments was conducted in a laboratory flume, in which flow field and bed surface topography at the grain-scale were measured. Two series of Particle Image Velocimetry (PIV) data in horizontal and vertical planes are coupled with bed topography measurements to provide a detailed description of near-bed flow and its connection to gravel-bed topography. Three different hydraulic scenarios with different relative submergence and aspect ratio, all within the range of intermediate submergence corresponding to flow type II, have been studied. Specifically, the main objectives of the paper are:

1. To identify pertinent features of open-channel flow (type II) over a gravel-bed, paying particular attention to the structure of the near-bed region.
2. To identify relations between the near-bed flow structure and bed topography at both depth scale and grain scale.

2. Methods and Data

The experiments were conducted in a 0.4 m wide, 0.4 m deep, and 6 m long polymethylmethacrylate rectangular tilting open channel (Figure 2a) at the Hydraulic Engineering Laboratory of the University of Trento. The flume bed was covered by a layer of gravel 20 cm thick. The flow depth was controlled by an adjustable tailgate installed at the end of the flume. The discharge at the flume inlet was controlled by an inverter for pump speed regulation, and was measured by an electromagnetic flowmeter. In our study, we employ the right-hand coordinate system, i.e., the x-coordinate is oriented along the main flow positive downstream and parallel to the mean bed, with its origin $x = 0$ located 3.3 m from the flume inlet; the z-coordinate refers to the vertical direction, pointing upward from the gravel tops (the z origin will be explained below); and the spanwise y axis is directed to the left wall (Figure 2b).

Gravel material with $D_{50} = 22$ mm and $D_{90} = 29$ mm (D_{50} and D_{90} are the particle diameters at 50% and 90% passing) was spread uniformly on the channel bottom to create a homogeneous gravel-bed layer (Figure 2c). The gravel-bed surface was smoothed mechanically by moving a wooden leveling table along a longitudinal guide from upstream to downstream, in order to avoid gravel clustering and produce conditions similar to water-worked gravel beds [e.g., *Aberle and Nikora*, 2006]. The bed topography was measured by a M5L/200 laser scanner (linearity error = 600 μm, distance resolution = 60 μm, and a spatial resolution = 1.5 mm^2) from $x = -200$ mm to $x = +300$ mm, covering a bed region above which velocity measurements were made. The effects of the measurement errors on the subsequent analysis were minimized using range validation and median filters, and then the least square fitting method was applied to remove the planar trend of the bed topography. The final bed topography after filtering and detrending is shown in Figure 2b.
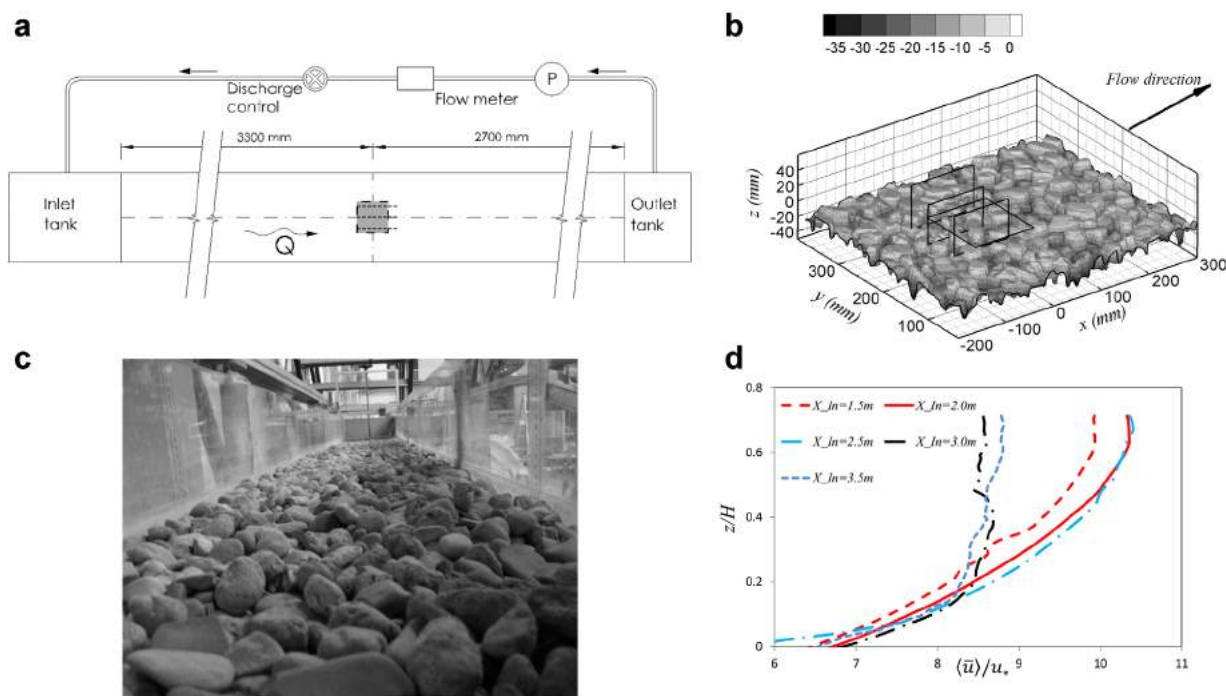
Figure 2. (a) Sketch of the open-channel flume; (b) relative location of the PIV vertical planes and horizontal plane above the gravel bed; (c) photograph of the gravel bed; and (d) spanwise-averaged streamwise velocity profiles (in this figure, X_In is measured from the flume inlet).

From the obtained data, the standard deviation of gravel bed elevations σ_I, which is a representative roughness scale (i.e., we assume $\Delta = \sigma_I^I$, *Nikora et al.* [1998a]) was estimated as 6.1 mm.

Three experimental scenarios (named Run I, Run II, and Run III) were studied, covering a range of hydraulic conditions while maintaining the Froude number almost constant (Table 1).

In Table 1, dimensionless vertical roughness length scale $\Delta^+ = u_* \sigma_I / v$ (where v is water kinematic viscosity, and u_* is the shear velocity) well exceeds 150, i.e., much larger than 5 which is an estimate of dimensionless viscous sublayer thickness [*Mayes et al.*, 2003]. This means that the studied flows exhibited a hydraulically rough bed condition. The relative submergence H_o / σ_I^I spanned from 7.5 to 10.8 showing that all three experimental flows can be defined as flows at intermediate submergence, i.e., flow type II. In all cases, the aspect ratio B/H was higher than 5 suggesting that effects of secondary currents in the central part of the flow should not be significant [*Nezu and Nakagawa*, 1993]. Free surface profiles along the whole flume length were measured by an ultrasonic distance transducer with 20 cm sampling interval, along the channel centerline. Uniform flow conditions were checked by comparing water surface slope to bed slope (S) which ranged within 0.0026–0.0029 (Table 1). Flow development lengths X_L for the three runs were estimated as in *Nikora et al.* [1998b] using a concept of the internal boundary layer of *Monin and Yaglom* [1971] and are reported in Table 1. To directly verify this estimate, velocity profiles were measured with UVP (Ultrasonic Velocity Profiler, MET-FLOW-SA) at five cross-sections along the flow and at seven transverse locations at each cross section. The comparison of the double-averaged velocity profiles at different longitudinal distances, shown in Figure 2d, demonstrate that profiles at $X\_In = 3.0$m and $X\_In = 3.5$ m, where X_In is the distance from the flume inlet, are almost overlapping, thus indicating that the flow after $X\_In = 3.0$m is in fully developed state.

Table 1. Hydraulic Conditions of Experimental Runs[a]

-	Run I	Run II	Run III
H (m)	0.040	0.052	0.060
S	0.0028	0.0026	0.0029
Fr	0.51	0.47	0.51
Δ^+	170	201	250
$Re_H \times 10^3$	12.75	17.63	23.32
B/H	10.0	7.7	6.7
Q (10^{-3} m³/s)	5.1	7.05	9.33
X_L (m)	1.37	1.61	1.74
H_o/σ_I	7.5	9.5	10.8

[a]S: channel slope, $Fr = U/\sqrt{gH}$: Froude number where g is acceleration of gravity and $U = Q/BH$ is mean velocity, $Re_H = UH/v$: Reynolds number, and Q: water discharge.

Table 2. Shear Velocity Estimates[a]

Experiment	u_m (m/s)	u_* (m/s)
Run I	0.033 ± 0.001	0.028 ± 0.006
Run II	0.036 ± 0.001	0.033 ± 0.003
Run III	0.041 ± 0.001	0.041 ± 0.009

[a]The shear velocity based on the Reynolds stress extrapolation has been obtained using data from all three measurement PIV planes.

Table 2 shows the local shear velocity u_* obtained by extrapolation of the Reynolds shear stress data to gravel particle crests using PIV measurements (as described below), and the global shear velocity u_m, obtained from the momentum balance as $u_m = (gHS)^{0.5}$. Estimated shear velocities differ within 17%, with a tendency for u_m to be larger than u_*, as one would expect [*Pokrajac et al.*, 2006]. As the estimate of the von Kàrmàn constant at intermediate submergence may be affected by relative submergence [e.g., *Gaudio et al.*, 2010], a shear velocity based on the logarithmic law was not estimated.

Measurements were performed in a flow region at least 150 mm far from both side walls at the distance of 3.3 m from the entrance of the channel (Figure 3a), where the velocity profile is fully developed while the effects of the downstream weir remain negligible. Two series of time-resolved PIV measurements were carried out.

In the first series of measurements, stereo PIV was applied to measure three velocity components (streamwise *u*, spanwise *v*, and vertical *w*) in the *x-y* (horizontal) plane located 1 mm above the roughness crests (i.e., 2-dimensional 3-component PIV, 2d3c, Figures 2b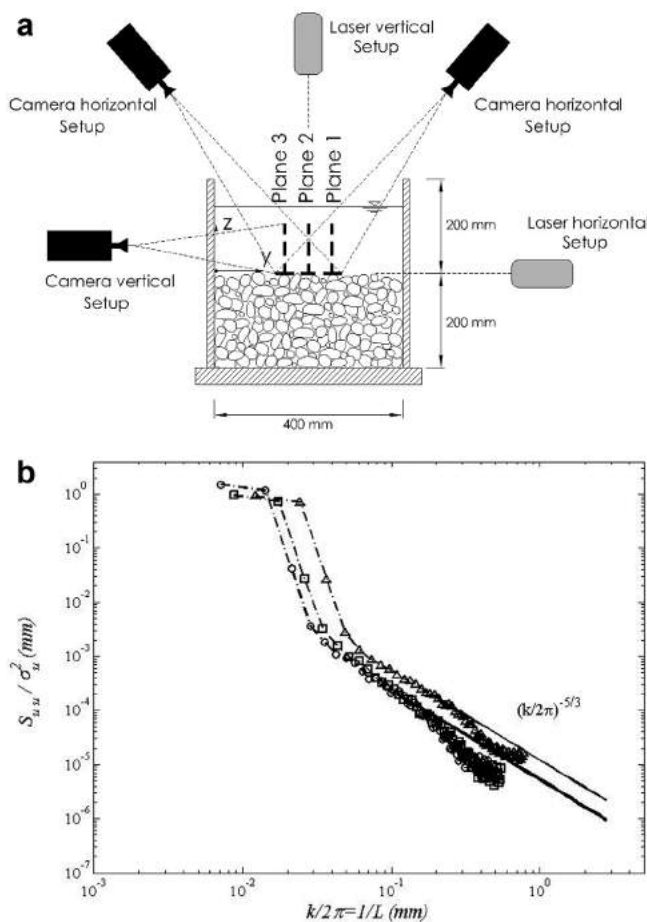 and 3a). In this mode, high-speed cameras were installed above the channel in a symmetric 45° configuration, using a water surface prism to avoid optical disturbances, and the laser sheet was aligned horizontally. To check that the surface prism did not affect the measurements, the thickness of the layer, which is affected by the surface prism presence, is estimated using a concept of the boundary layer theory and available formulas for turbulent boundary layer thickness [*Mayes et al.*, 2003]. Estimated boundary layer thickness shows that in all three runs only a thin near-water-surface layer (10% of the water depth) could be affected by the surface prism and thus PIV measurements near the gravel bed are not affected by the prism. The acquisition area was approximately 140 mm long and 140 mm wide, with its center placed approximately at the middle of the channel (Figures 2a, 2b, and 3a). In the second series of measurements, 2-dimensional 2-component (2d2c) PIV was used to measure flow fields at three vertical *x-z*-planes located at the centerline, 50 mm left, and 50 mm right of the channel center, as shown in Figures 2b and 3a (and also in Figures 6 and 7). The camera was placed at the left side of the

Figure 3. (a) Streamwise view showing both conventional 2-component and stereoscopic 3-component PIV set-ups; (b) one-sided normalized velocity spectra (S_{uu}) from PIV data; bold line indicates extrapolation of spectra to 3η where η is the Kolmogorov dissipative scale, estimated following *Nezu and Nakagawa* [1993], page 30; triangle—Run I, square—Run II, circle—Run III. The spectra are normalized as velocity variance (σ_u^2).

channel and the laser beam came from the top of the channel, directed through a prism to avoid potential water surface effects.

In all measurements, high-speed Fastcam X 1024 PCI Photron cameras with a super light sensitive 10-bit CMOS sensor were used. The laser was a Nd : Yag in continuous mode. Sieved pollen particles (particle size of 0.075–0.125 mm and particle density of 1.07 g/cm^3) were used as seeding material. For each run, the diluted seeding material was injected at the entrance of the channel. The volumetric concentration of pollen particles (PIV targets) and the contrast between the white target spots and the image background were adjusted to obtain a homogeneous distribution of the particles, especially near the bed region. To eliminate the domains occupied by the bed in the images, a mask based on the measured bed elevations was prepared and applied to the data. The measurement regions were 1024×512 px$^2 \approx 128 \times 64$ mm^2 in the vertical planes and 1024×1024 px$^2 \approx 140 \times 140$ mm^2 in the horizontal plane. For each run, in total three vertical planes covered at least 12 large bed gravel particles along the x direction.

The image analysis and processing were performed with PIVDEF software (CNR-INSEAN) [*Di Florio et al.*, 2002]. At first step, the minimum value of image intensity was subtracted from PIV recordings in order to reduce the effects of laser flare. The flow field was then reconstructed by the iterative cross-correlation method with smallest interrogation window of 32×16 (75% overlap) in the vertical planes and 28×28 (50% overlap) in the horizontal plane, by applying the window deformation and subpixel refinement technique [*Scarano*, 2002]. Also, in order to reduce the number of spurious vectors, a four point (2×2) local median filter [*Westerweel and Scarano*, 2005] was applied to the measured data. In the horizontal plane, the 2-D3c reconstruction was performed using 332° polynomial mapping function proposed by *Soloff et al.* [1997].

The resulted vector spacing (l_{IA}) was approximately 1 mm in both horizontal and vertical planes. For each experiment, the sampling frequency was 500 Hz. Flow was sampled for 38.4 s in vertical-plane measurements and for 13 s in horizontal-plane measurements. Comparison of our set-up with *Cooper and Tait* [2010] findings, who specifically studied the effects of PIV set-up on velocity statistics over gravel beds, shows that the measurement durations in the vertical planes were long enough to ensure statistical convergence for at least low-order moments of the flow field. Although the measurement duration in the horizontal plane seems fairly short for obtaining the reliable statistics, it appears sufficient for our analyses as its spatial equivalent exceeds 60 flow depths (Taylor's frozen turbulence hypothesis was used here for converting time domain into spatial domain). The ratio of the vector spacing to the bed material size (l_{IA}/D_{50}) in the present study is approximately 0.05 allowing analysis of the flow structure at a subparticle scale, which was not reported in the previous studies.

It has been shown that if the ratio of a tracer particle diameter to the size of a CCD pixel in the image is larger than three to four, the uncertainty of the displacement measurement is of the order of one-tenth to one-twentieth of the particle diameter [*Prasad et al.*, 1992]. However, for better understanding of measurement errors in our PIV data, a spectral analysis was conducted as suggested in *Detert* [2008]. Based on his method, the quality of measured PIV data can be estimated by the ratio of the resolved (measured) turbulent energy to the total turbulent energy [*Detert et al.*, 2010; *Weitbrecht et al.*, 2011]. The resolved turbulent energy is estimated from the area under the experimental spectral curves while the total turbulence intensity can be obtained by extrapolation of experimental spectra to Kolmogorov length scale [*Lavoie et al.*, 2007]. Figure 3b shows the normalized wave-number spectra using velocity variance (estimated using Welch's method) of streamwise velocity at $z/H = 0.4$ of the center-line vertical plane. The estimates demonstrate that at least 96% of turbulent energy is retrieved from the measurements. Finally, 95% confidence level sampling errors, assuming normal distribution for measured variables [*Benedict and Gould*, 1996], are given in Table 3.

3. Gravel-Bed Characteristics

Before presenting the data on the flow field, it is useful to describe the quantitative properties of the bed in more detail. This approach allows a comparison of the present laboratory gravel bed with the previously studied natural water-worked and artificially created beds. Also, it can be helpful for understanding the relation of gravel bed characteristics with the flow field. The size distribution curve of bed materials is shown in Figure 4a. To produce this curve, three axes of each particle (longest a, intermediate b and shortest c) from

Table 3. 95% Relative Sampling Errors of Turbulence Parameters

	Vertical Planes (%)			Horizontal Layer (%)		
	Run I	**Run II**	**Run III**	**Run I**	**Run II**	**Run III**
$\bar{u}$	0.90	0.83	0.91	1.13	1.84	1.81
$\bar{v}$				8.60	13.11	25.25
$\bar{w}$	28.14	24.41	30.36	15.91	15.28	29.87
σ_u	2.34	2.68	2.57	2.42	3.03	2.94
σ_v				1.62	2.12	2.03
σ_w	1.40	1.53	1.49	2.21	2.29	2.21
$-u'w'$	0.43	0.53	0.51	0.75	1.05	0.89

bed material of sample around 10 kg were measured. The particle size shown in Figure 4a is defined as ($\sqrt[3]{abc}$). The standard deviation of the particle size distribution σ_G which is estimated as $\sigma_G = \exp((\ln D_{16}/\ln D_{84})/4 + (\ln D_5/\ln D_{95})/6.6)$ (D_x are the particle diameters at $x\%$ passing) [*Folk and Ward*, 1957] was estimated to be 0.82 mm. This value of σ_G, together with Figure 4a, shows that the size distribution curve of bed material is fairly narrow. A consideration of three particle axes a, b, and c shows that the bed particles were generally spherical (46%), although the bed also included stones of blade (25%), disc (18%), and roller (11%) shapes [*Selley*, 2000]. However, on average shape factor ($SF = \bar{c}/\sqrt{\bar{a}\bar{b}}$) is 0.52 (overbar means averaging over the whole sample).

The histogram of bed surface elevations z_{bed}, measured by the laser scanner, is shown in Figure 4b. Bed elevation distribution has a mild negative skewness ($Sk = -0.4$) and its kurtosis value ($K = -0.02$) is close to
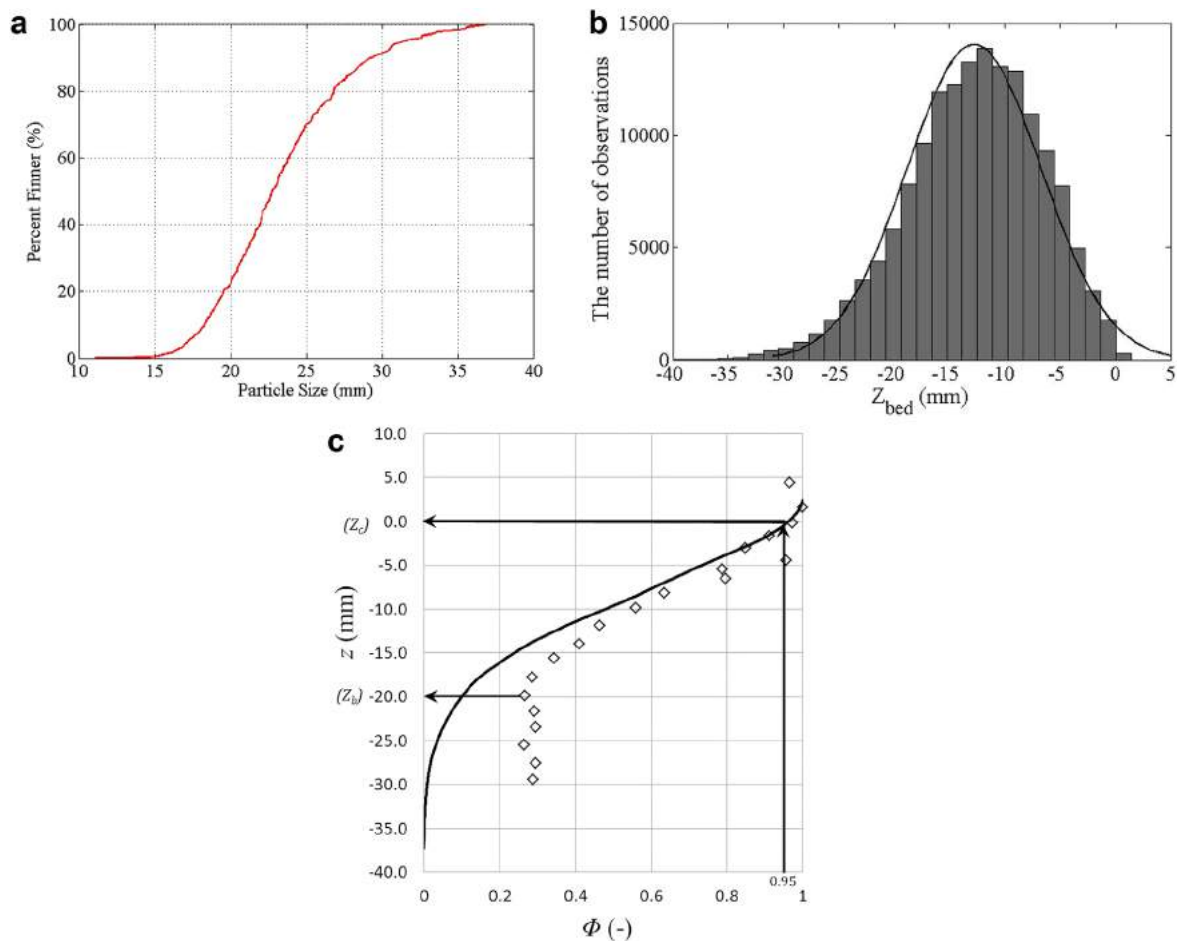

Figure 4. Gravel bed characteristics: (a) particle size distribution curve, particle size = $\sqrt[3]{abc}$; (b) histogram of bed surface elevations; and (c) porosity (roughness geometry) function Φ as measured with water displacement method (diamond) and with digital elevation method (black line).

zero. The Kolmogorov-Smirnov test shows that the normality hypothesis is rejected at a significance level of 0.01 due to the presence of negative skewness. Negative value of skewness could result from regularizing the gravel bed surface with the wooden leveling table. Indeed, the board smoothing would push down any positive elevations on the positive tail of the distribution. According to *Coleman et al.* [2011], similar values of *Sk* and *K* are expected for rough beds with random distribution of roughness elements like unworked gravel bed. However, it is worth noting that the skewness for water-worked beds is of the same magnitude but positive [e.g., *Nikora et al.*, 1998a].

In Figure 4c, the porosity function Φ is shown, which is defined as the ratio of the area occupied by fluid to the total area of the averaging domain that includes, below roughness crests, the gravel particles. The porosity function evaluated by two different methods: (1) elevation distribution method; and (2) water displacement method [*Aberle*, 2007]. The first method is based on the digital elevation model of the bed topography. In the second method, water was filled stepwise into the gravel bed and Φ was calculated from the volume of the added water and the associated increment of the water levels [*Aberle*, 2007]. A similar method traditionally is used for determination of the zero-bed elevation [*Flintham and Carling*, 1988]. The mean bed level Z_m was 12.7 mm lower than the gravel crest level Z_c, defined as the elevation corresponding to 95% of cumulative frequency of measured bed surface elevations. This Z_c level is defined as the origin of the vertical coordinate z. As elevation distribution method does not consider the pore volume of the bed, the lower boundary of the roughness layer Z_b was determined as the level where the porosity function based on the water displacement method tends to become constant (Figure 4c).

Additional information on the bed surface organization can be extracted from the generalized structure functions of bed elevations [*Nikora et al.*, 1998a; *Nikora and Walsh*, 2004]. The generalized structure functions of surface elevations are defined as $D_p(\Delta x, \Delta y) = [|z(x+n\delta x, y+m\delta y) - z(x,y)|^p]$ where exponent p is the structure function order, $\Delta x = n\delta x$ and $\Delta y = n\delta y$ are longitudinal and transverse spatial lags, δx and δy are spatial sampling intervals, $||$ denotes absolute value, and $[]$ defines averaging over many point pairs [*Nikora and Walsh*, 2004]. Note that the second-order structure function is equivalent to the bed elevation variogram used in *Robert* [1991]. In the present study, the generalized longitudinal $D_p(\Delta x, \Delta y = 0) = [|z(x+n\delta x) - z(x)|^p]$ and transverse $D_p(\Delta x = 0, \Delta y) = [|z(y+m\delta y) - z(y)|^p]$ structure functions up to order five are calculated as well as the two-dimensional second-order structure function $D_p(\Delta x, \Delta y) = [|z(x+n\delta x, y+m\delta y) - z(x,y)|^2]$, which was estimated using 500 and 350 points in the longitudinal and transverse directions, respectively (Figure 5). As one can see in Figures 5a and 5b, both longitudinal and transverse structure functions reveal the existence of three ranges: scaling, transition, and saturation regions, as one would expect for gravel-bed surfaces [e.g., *Nikora et al.*, 1998a]. Within the scaling ranges at small spatial lags, the structure functions exhibit power-type behavior $D_p(\Delta x) \propto \Delta x^{\xi_{p_x}}$ and $D_p(\Delta y) \propto \Delta y^{\xi_{p_y}}$, with scaling exponents shown in Figure 5c as a function of the order p. Both exponents ξ_{p_x} and ξ_{p_y} nonlinearly depend on the structure function order suggesting multiscaling behavior [*Davis et al.*, 1994]. Similar results were reported by *Nikora and Walsh* [2004] for both natural water-worked and artificial unworked gravel surfaces.

Characteristic scales (L_x, L_y) of the gravel bed in the longitudinal and transverse directions can be defined based on $D_p(\Delta x)$ and $D_p(\Delta y)$ as spatial lags corresponding to the intersections of the scaling and saturation regions [*Nikora et al.*, 1998a]. Results for $D_2(\Delta x)$ and $D_2(\Delta y)$ are reported in Figures 5a 5b, and Table 4. The obtained values are in agreement with observations for laboratory and natural water-worked gravel beds showing that $L_x \approx 0.5D_{50}$ [*Nikora et al.*, 1998a; *Nikora and Walsh*, 2004; *Aberle and Nikora*, 2006]. The ratio of characteristic scales in the longitudinal and transverse directions L_x/L_y was found to be larger than one and approximately equal to the ratio of mean longest to mean intermediate particle axes $\bar{a}/\bar{b}$. This observation can be explained by the procedure used to the level gravel-bed surface that forced the particles to orient along the flow. Interestingly, similar orientation was noted by *Aberle and Nikora* [2006] for laboratory water-worked armored gravel surfaces.

The shape of the two-dimensional second-order structure function shown in Figure 5d is also similar to that reported for natural and artificial beds. For natural water-worked beds, it has been observed that contours of the structure function at small scales is circular, while at larger scales they become significantly elliptical with the maximum axis inclined with respect to the x axis [*Goring et al.*, 1999]. For laboratory water-worked gravel beds, *Aberle and Nikora* [2006] reported that the longest diameter of a contour ellipse in the two-dimensional second-order structure function was aligned in the x direction for small
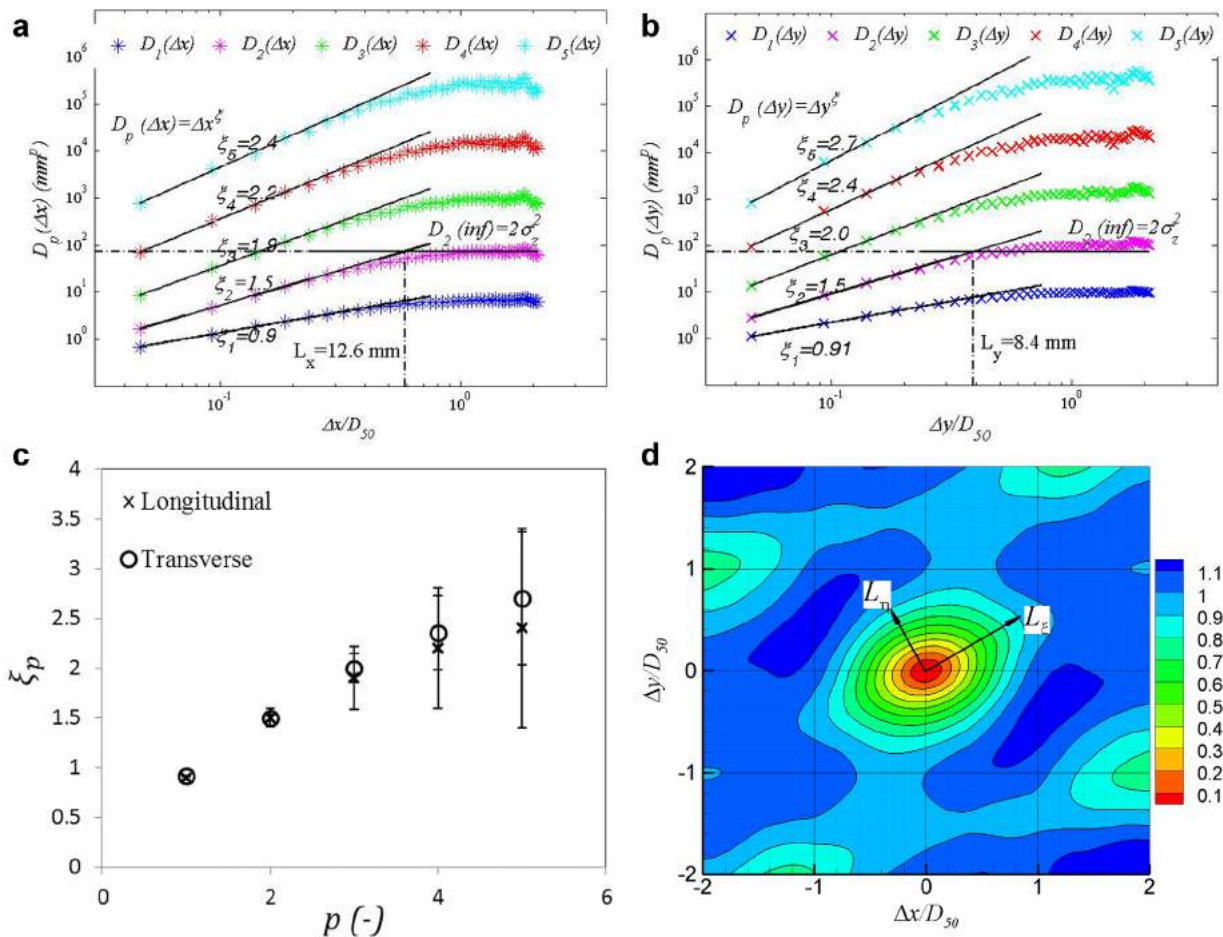
Figure 5. (a) High-order longitudinal structure functions; (b) high-order transverse structure functions; (c) scaling exponents of the generalized structure functions; and (d) contour map of the second-order structure function of bed elevations.

spatial lags, but inclined for larger lags. This observation was explained by different behavior of small particles compared with that of large particles during the armoring process. In the present study, as shown in Figure 5d, the shape of small-scale contour lines has a mild inclination with respect to the x axis, which increases for larger scales. To compare the longitudinal and transverse scales, the ratio of largest to smallest diameters of the ellipse of a contour line at the border of scaling and saturation region (L_ξ, L_η in Figure 5d) is calculated and reported in Table 4. The value of this ratio is close to that of longitudinal and transverse characteristic scales (L_x/L_y) and to that of mean longest to mean intermediate axes of bed particles ($\bar{a}/\bar{b}$).

In the present study, we attempted to produce conditions similar to the natural water-worked gravel beds by spreading gravels randomly on the channel bed and then "regularizing" them mechanically along the main flow direction. However, it was found that while some of the bed properties are very similar to natural water-worked beds (e.g., near-Gaussian distribution of bed elevations, structure function scaling, characteristic scales and their ratio, particle orientation), some differences are also observed (e.g., negative skewness of bed elevations compared with positive skewness expected for natural beds). Specifically, negative value of skewness together with near-zero value of kurtosis in present study is in agreement with unworked gravel bed

Table 4. Comparison of Longitudinal and Transverse Statistical Properties of Gravel Bed in Present Study

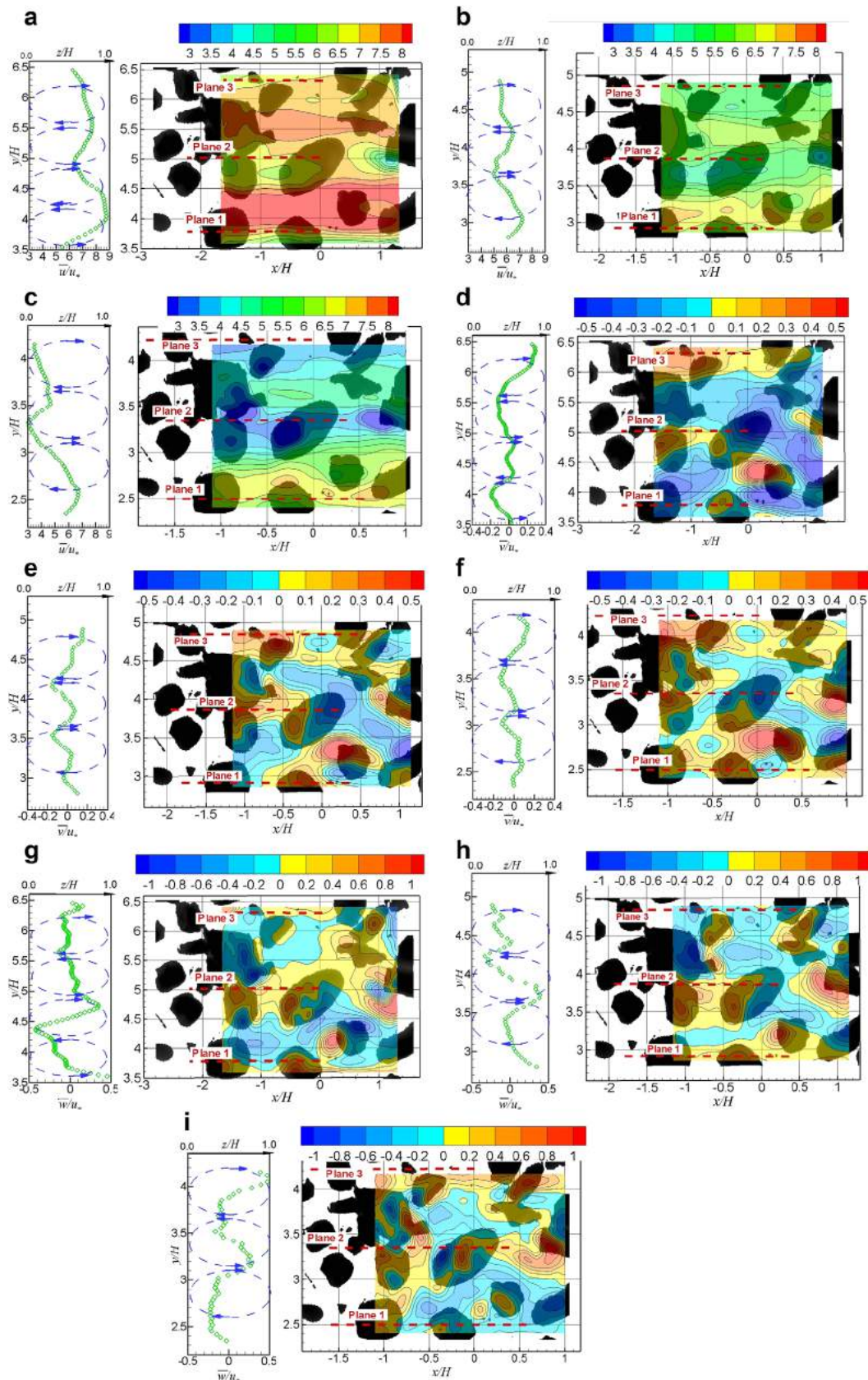|	Longitudinal	Transverse	Ratio
L_x, L_y (mm)	12.6	8.4	1.5
L_ξ, L_η (mm)	20.9	14.8	1.4
	Averaged Particles Diameters		
	Longest, $\bar{a}$ (mm)	Intermediate, $\bar{b}$ (mm)	Ratio
	30.1	22.00	1.4

Figure 6.

characteristics. In any case, the present gravel bed is fairly well quantified and can be reproduced in future studies.

4. Flow Structure

4.1. Turbulence Characteristics in a Horizontal Near-Bed Plane

In Figure 6, color contour maps of time-averaged velocity components in the horizontal plane at 1 mm above the roughness crests (i.e., $z_{plane}=1$ mm where z_{plane} is the vertical distance of the horizontal plane from the z-origin) are shown. This presentation means that the relative distance of the horizontal measurement plane from the origin (z_{plane}/H) is slightly different for Runs I, II, and III ($z_{plane}/H=0.025$ in Run I, $z_{plane}/H=0.019$ in Run II, and $z_{plane}/H=0.017$ in Run III). All velocity components are normalized by u_* from Table 2. For comparison, the bed topography above Z_m is shown in the background. The distribution of the streamwise velocity $\bar{u}/u_*$ for all three runs in Figures 6a–6c reveal the existence of low and high velocity strips alternating in the spanwise direction. Cores of high velocity strips are up to 10% faster than the surrounding flow. Contour maps of the spanwise velocity $\bar{v}/u_*$ (Figures 6d–6f) and vertical velocity $\bar{w}/u_*$ (Figures 6g–6i) also reveal longitudinal strips of positive and negative velocities, although weaker when compared to $\bar{u}/u_*$. These data suggest that the observed strips are likely to be the signatures of turbulence-induced secondary currents [*Nezu and Nakagawa*, 1993]. It can be also noted that gravel protrusions interfere with the streaky structure of the velocity contour maps. In addition to the contour maps, left-side parts of the plots in Figure 6 show spanwise profiles of the time and longitudinally averaged velocities of all three velocity components, accompanied with idealized sketches of corresponding helical cells that may generate such low-momentum and high-momentum strips. The lower horizontal axis of these parts of the plots relates to the longitudinally averaged velocity and the upper horizontal axis is z/H shown for visualization of the helical secondary cells. The data suggest that the strips of negative w-component (downflow) correspond to high streamwise velocity strips, while the strips of positive w-component (upflow) correspond to low streamwise velocity strips. Moreover, there is a tendency of changing sign of $\bar{v}$ at the transverse locations where streamwise and vertical velocities attain minimums or maximums (Figures 6d–6f). This behavior is consistent with convergence and divergence of transverse fluid motions due to the secondary currents. The lateral spacing of streamwise velocity strips is in the range 1.2–1.6 water depths, which is somewhat smaller than those measured by *Kinoshita* [1967] (2*H*) in a wide river and *Albayrak and Lemmin* [2011] (1.85*H*) in a laboratory open channel. Similar to the streamwise velocity, strip spacing in the patterns of the vertical and spanwise velocity components were found to be within the same range (1.2–1.6*H*).

As already mentioned, it can be also seen that the low-momentum and high-momentum strips in Figure 6 are disrupted, at least partly, by the protrusions of gravel particles. The effect of particle protrusions is different for different velocity components. As far as the streamwise velocity is concerned, gravel particle protrusions form regions of flow deceleration and lower velocity (wake zones) at the lee of some particles (Figures 6a–6c). The vertical velocity is mostly positive at the upstream sides of gravel crests, depending on particle shape, orientation and the arrangement of surrounding particles. In the downstream side of gravel crests, the vertical velocity is typically negative (Figures 6g–6i). In the case of the spanwise velocity, strong variations are observed around each gravel particle, again depending on the particle shape and orientation. Moreover, it seems that the variations of the spanwise velocity reflect some bending of low and high-momentum "strips" around bed protrusions, which is particularly evident in Run III.

The presence of the secondary currents and bed topography effects are also visible in the turbulence statistics. As an example, Figure 7 shows the streamwise and vertical turbulence intensities σ_u/u_* and σ_w/u_* for Run I and Reynolds shear stress ($-\overline{u'w'}/u_*^2$) for Run I and Run III. The turbulence intensities and Reynolds stress contour maps in Figure 7 reveal some transverse variations too, with strip spacing comparable to those noted in the maps of the time-averaged velocity components. However, strip structures in the second-order moments are less profound, especially for the vertical turbulence intensity. Surprisingly, despite the fact that the aspect ratio reduces from Run I to Run III (Table 1), the transverse variation of $-\overline{u'w'}/u_*^2$ caused by secondary currents is less clear in Run III than in Run I. The tendency for

Figure 6. Contour maps of velocity components in the horizontal plane just above the particle crests: (a) $\bar{u}/u_*$, Run I; (b) $\bar{u}/u_*$, Run II; (c) $\bar{u}/u_*$, Run III; (d) $\bar{v}/u_*$, Run I; (e) $\bar{v}/u_*$, Run II; (f) $\bar{v}/u_*$, Run III; (g) $\bar{w}/u_*$, Run I; (h) $\bar{w}/u_*$, Run II; and (i) $\bar{w}/u_*$, Run III. Flow from left to right. Left-side subplots show both transverse distribution of the time and longitudinally averaged velocities and sketches of secondary currents in the z-y plane. Note that the origin of the x axis is within the measurement window.
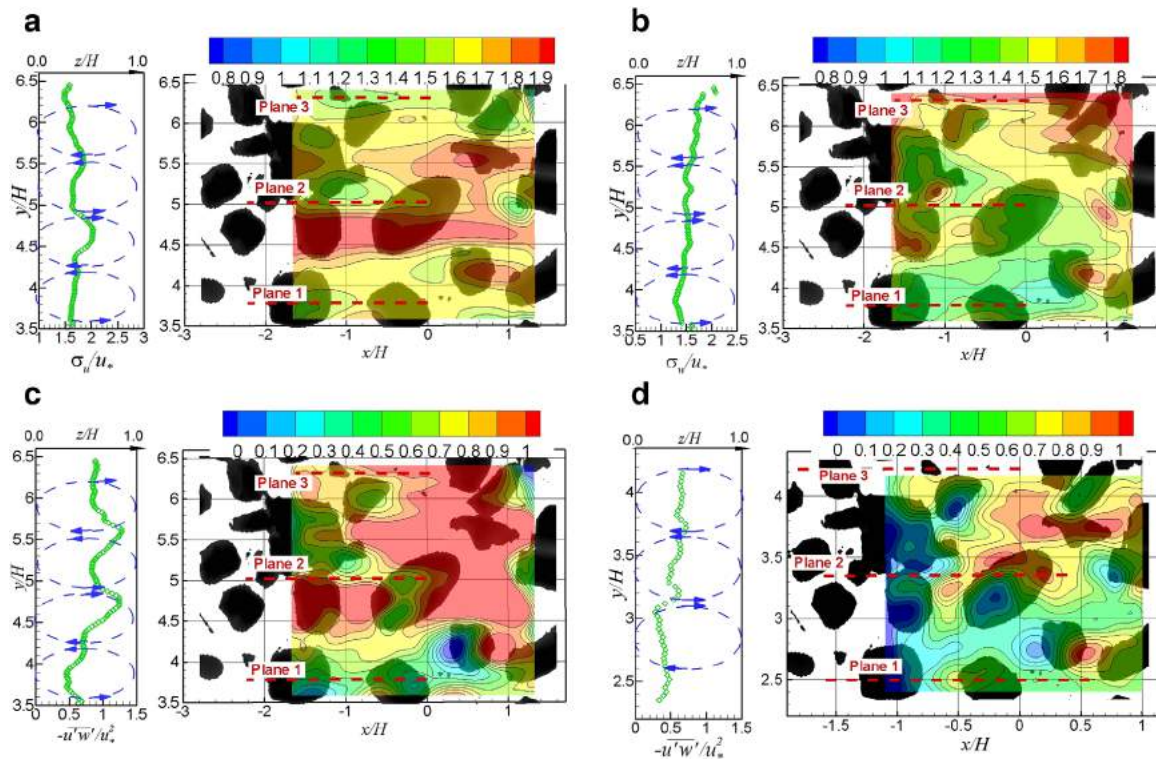
Figure 7. Contour maps in the horizontal plane just above the particle crests for: (a) σ_u/u_* (b) σ_w/u_*; (c) $-\overline{u'w'}/u_*^2$ for Run I; and (d) $-\overline{u'w'}/u_*^2$ for Run III. Flow is from left to right. Note that the origin of the x axis is within the measurement window.

"weakening" the strip structure with increasing relative submergence is noticed for all turbulent intensity and Reynolds stress data (not shown), similar to the study of *Cooper and Tait* [2008]. The interpretation of this effect is not straightforward because we have to compare measurements at a fixed elevation just above the crests but at a range of flow depths, i.e., at different relative distances z_{plane}/H from the roughness crests (as in *Cooper and Tait* [2008]). In other words, as mentioned at the beginning of this section, the actual "submergence" of the measurement plane into the roughness layer ($H-z_{plane}$) was increasing with increasing relative submergence, i.e., it increased from Run I to Run II to Run III. It is fair to expect that the roughness layer obscures the signatures of the secondary currents near the bed and that this effect should be getting stronger toward to bed. This explanation seems quite plausible and in full agreement with plots in Figures 6 and 7. In addition to the large-scale strips, the contour maps of the second-order moments also reveal smaller-scale variations due to the local effects of gravel-bed topography, which "weaken" the appearance of the strips. This feature can be observed in Figure 7, in which regions of strong turbulence intensities are seen at the lee of gravel particles if particle spacing is sufficiently large for a wake to develop. The small-scale variation of the Reynolds stress is similar to that of the turbulence intensities, i.e., it also exhibits high local values at the lee of the bed particles.

4.2. Turbulence Characteristics in Vertical Planes

Velocity contour maps in vertical measurement planes supplement findings based on the horizontal plane measurements described above. The contour maps for the streamwise velocity in Figure 8 show that the flow can be subdivided into two regions: (1) the near-bed region of high heterogeneity in the mean velocity field, occupying a layer from the roughness crests to the level $z \approx \sigma_I$; and (2) the upper flow region (above $z \approx \sigma_I$) where velocity field is almost homogenous. One may observe that the near-bed variation of velocity field is mainly due to gravel particle protrusions. As with the data for the horizontal measurement plane, the streamwise velocity in the vertical plane reduces at the lee of gravel particles. The reduction of velocity is consistent with the wake formation in the space between surrounding particles. These observations are in agreement with previous studies which also showed that the near-bed velocity field is highly affected by gravel bed topography [*Hoover and Ackerman*, 2004; *Hardy et al.*, 2010; *Mignot et al.*, 2009]. A thorough
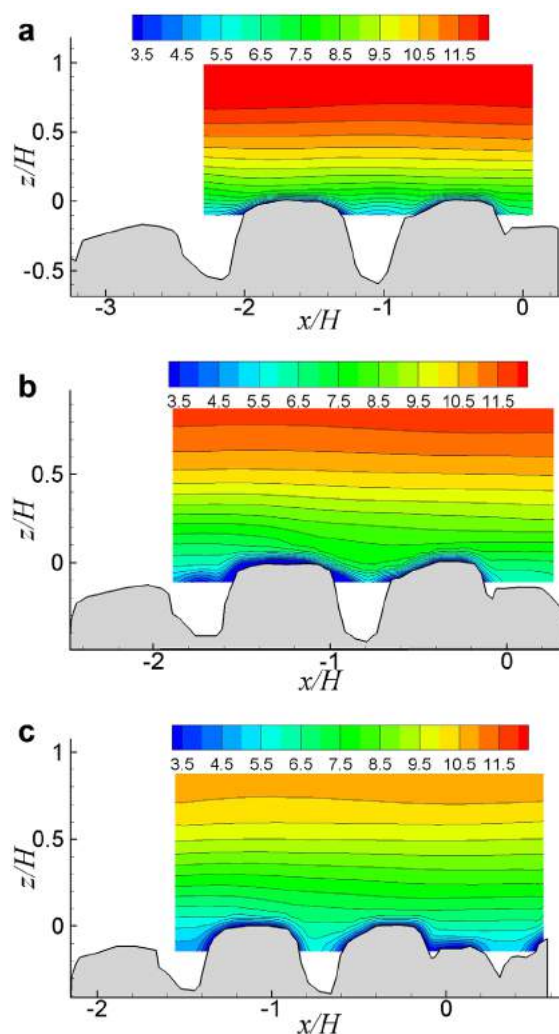
Figure 8. Contour maps of $\bar{u}/u_*$ in the vertical plane 1 for (a) Run I; (b) Run II; and (c) Run III. Flow from left to right. Note that the origin of the x axis is within the measurement window.

comparison of the contour maps in the horizontal and vertical planes shows that there are slight differences between velocity statistics at the interceptions of horizontal and vertical planes (i.e., where velocity statistics ideally should be the same). As an example, in Figure 8b in the middle of plane 1, there is a region between two particles where $\bar{u}/u_* \approx 7$. However, in Figure 6b one can observe that the ratio $\bar{u}/u_*$ between the same particles is slightly smaller than 7. The error analysis showed that the observed differences are within standard errors (e.g., standard error of $\bar{u}/u_*$ in Figures 6b and 8b is within 0.7–1.0, which is higher than the observed differences).

Figure 9 reports the contour maps of measured turbulence intensities and the primary Reynolds stress in the same plane as in Figure 8. Similar to the mean velocity field, the near-bed region is highly heterogeneous, while the region far away from the bed is fairly homogeneous. However, compared to the mean velocity field, the heterogeneous near-bed region for the second-order moments is appreciably thicker, i.e., about $2.5\sigma_l$. Thus, Figures 8 and 9 suggest that the thickness of the near-bed heterogeneous region strongly depends on a parameter under consideration. In all contour maps of Figure 9, the patchiness in the spatial distribution of near-bed flow parameters is mostly associated with protrusions of particle crests and with troughs between them. Checking Figure 9, one can also see that the relative turbulence intensities generally increase with t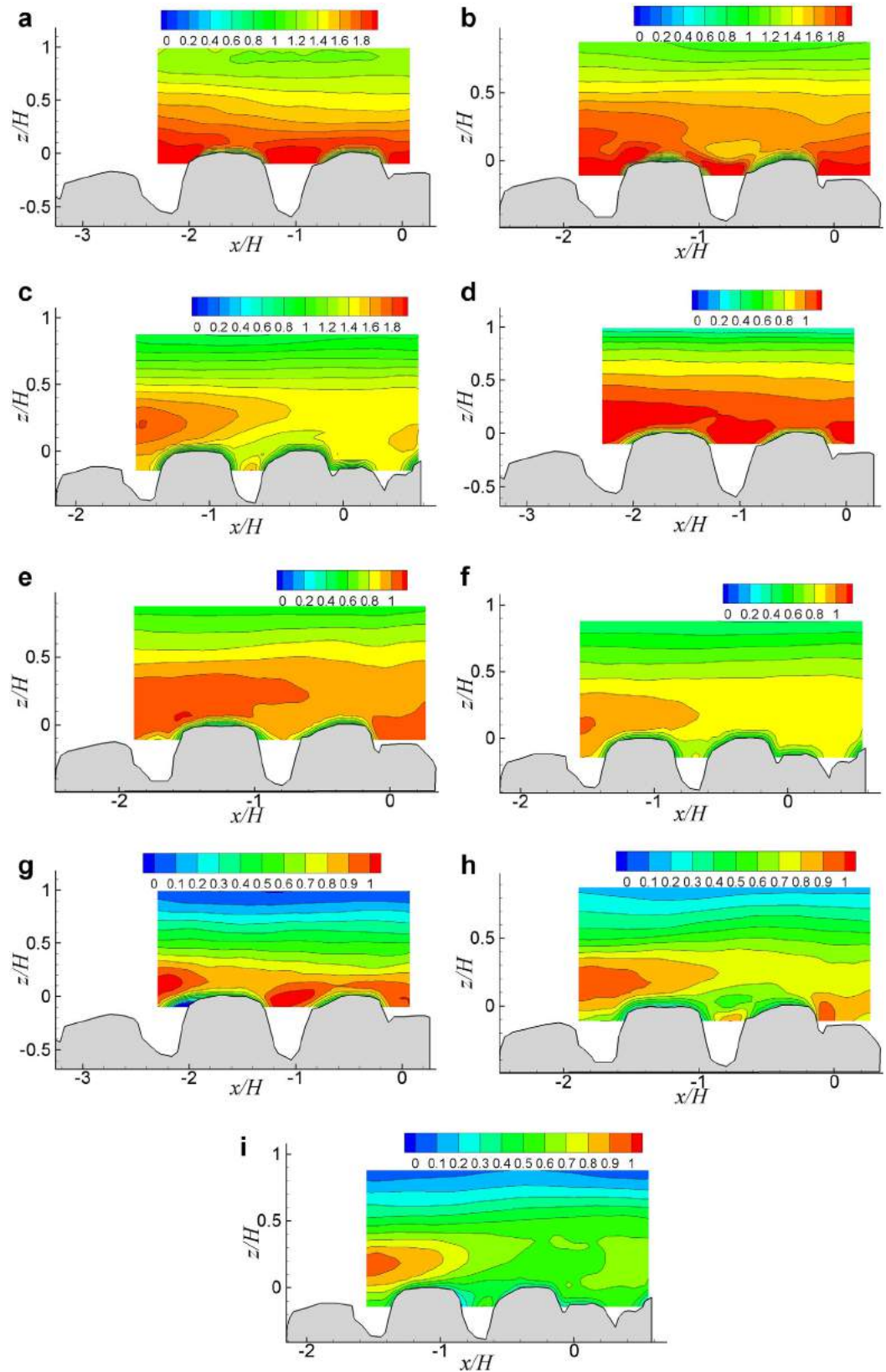he decrease in flow submergence. In addition, it can be noticed that for Run I a distinct maximum is present behind the upstream particle, in analogy to what could be expected in the wake of a bluff body [see e.g., *Braza et al.*, 2006; *Dong et al.*, 2006]. However, this maximum tends to reduce with increase in flow submergence in Runs II and III. These results are consistent, at least partially, with those reported by *Hardy et al.* [2009]. They found that for a low Reynolds number flow the strength of wakes behind gravel particles is higher than that for flow at high Reynolds number. Therefore, the overall spatial heterogeneity of the near-bed turbulence increases with decreasing Reynolds number. At high Reynolds numbers, the skimming near-bed flow tends to prevail. Nevertheless, there is a difference between our findings and that of *Hardy et al.* [2009]. They showed that the turbulence intensity increases with Reynolds number while in the present study the local maxima are higher for lower submergences and thus for lower Reynolds numbers. This apparent disagreement will be addressed in the Discussion section.

4.3. Vertical Distribution of Double-Averaged Flow Quantities
The profiles of the spatially averaged Reynolds shear stress $-\langle \overline{u'w'} \rangle$ for all three measurement planes in Run II are given in Figure 10 (the plane locations are shown in Figures 6 and 7). One can see that the stress profiles in planes 1 and 2 are convex and the experimental points tend to be located above the expected theoretical linear profile of 2-D flow [e.g., *Nezu and Nakagawa*, 1993]. In contrast, the $-\langle \overline{u'w'} \rangle$ profile in plane 3 is concave near water surface and convex near the bed, although the experimental points are

Figure 9. Contour maps of turbulent intensities and the primary Reynolds stress in the vertical plane 1: (a) σ_u/u_* for Run I; (b) σ_u/u_* for Run II; (c) σ_u/u_* for Run III; (d) σ_w/u_* for Run I; (e) σ_w/u_* for Run II; (f) σ_w/u_* for Run III; (g) $-\overline{u'w'}/u_*^2$ for Run I; (h) $-\overline{u'w'}/u_*^2$ for Run II; and (i) $-\overline{u'w'}/u_*^2$ for Run III. Flow is from left to right. Note that the origin of the x axis is within the measurement window.
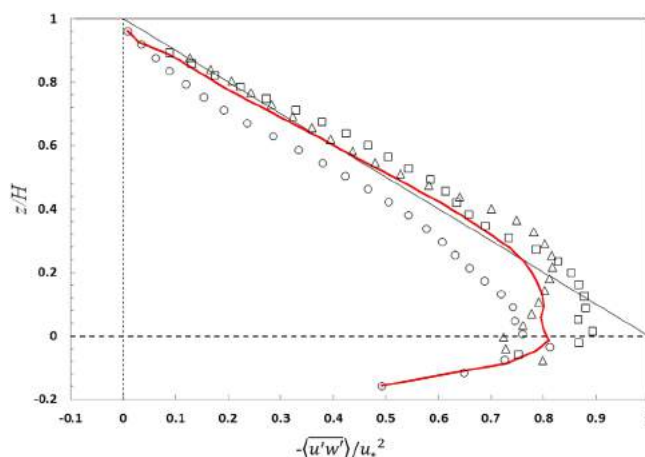
Figure 10. Spatially averaged Reynolds shear stress profiles for Run II: triangle—plane 1; square—plane 2; circle—plane 3; red line relates to the Reynolds stress averaged over all three planes.

located below a linear profile. The plots of $-\langle \overline{u'w'} \rangle$ are consistent with the presence of secondary currents which cause deviation of the $-\langle \overline{u'w'} \rangle$ distribution from the 2-D linear distribution [*Nezu and Nakagawa*, 1993; *Albayrak and Lemmin*, 2011]. Indeed, measurement planes 1 and 2 are located in the regions where upward fluid motion are predominant, while plane 3 is in the downward flow region (Figure 6), in agreement with the results for secondary currents [*Nezu and Nakagawa*, 1993; *Nikora et al.*, 1998b; *Albayrak and Lemmin*, 2011]. Differences in the $-\langle \overline{u'w'} \rangle$ profiles due to the secondary currents highlight the importance of considering this phenomenon when perform-

ing the double-averaging analysis of rough-bed open-channel flows. In the present study, the double averaging is employed using two averaging domains: (1) a thin narrow slab with the length equal to the measurement window length, width equal to the laser sheet width, and thickness equal to the vector spacing in PIV analysis (i.e., averaging is performed separately for individual planes); and (2) a thin wide slab having the length equal to the measurement window length, width equal to the transverse distance between planes 1 and 3, and the thickness equal to the vector spacing in PIV analysis. First option provides double-averaged quantities that account for particle-scale heterogeneity but may spatially vary due to the effects of secondary currents. The second option involves averaging the data from all three measurement planes. Of course, the quality of this averaging is not high but at least some heterogeneity induced by the secondary currents is accounted, in addition to smaller-scale heterogeneity due to gravel particles. The red line in Figure 10 represents the Reynolds stress profile averaged over all three planes, following option 2 that accounts for both types of heterogeneity: due to secondary currents and due to smaller-scale effects of gravel particles. Interestingly, the red line is close to a linear distribution expected for 2-D open channel flows.

As mentioned in the Introduction, some data suggest that the shape of the double-averaged velocity profile in flows of intermediate submergence (i.e., flow type II) follows a logarithmic formula:

$$\frac{\langle \overline{u} \rangle}{u_*} = \frac{1}{\kappa_{(\Delta/H_o)}} \ln \left(\frac{z-d}{\Delta} \right) + C = \frac{1}{\kappa_{(\Delta/H_o)}} \ln \left(\frac{z-d}{z_o} \right) \tag{1}$$

where κ is von Kàrmàn constant, d is the zero-plane displacement, z_o is the hydrodynamic roughness length, and C is an additive constant. Note that in equation (1) subscript Δ/H_o highlights potential dependence of κ on the relative submergence. In this study, the roughness scale Δ in equation (1) is assumed to be the standard deviation of bed elevations σ_I. Estimation of the parameters of the log-law and identification of its spatial bounds is not straightforward for flow type II. Following *Nikora et al.* [2002], this information can be extracted from an equation:

$$(d\langle \overline{u} \rangle/dz)^{-1} = \frac{\kappa}{u_*} z - \frac{\kappa}{u_*} d \tag{2}$$

which is valid only in the logarithmic region. Thus, the bounds of the log-law can be assumed as a region where equation (2) applies. Then, d can be determined as the ratio of the intercept to the slope of the linear regression equation in the logarithmic region, without a need for a shear velocity estimate [*Nikora et al.*, 2002]. The von Kàrmàn constant can be obtained from an equation:

$$\kappa = \frac{u_*}{(z-d)} (d\langle \overline{u} \rangle/dz)^{-1} \tag{3}$$

Once d is estimated from equation (2) and u_* is estimated from the spatially averaged Reynolds stress profile, equation (3) may be used as an additional diagnostic tool to check the bounds of the log-law (i.e., Z_L

Table 5. Summary of Estimated Zero-Plane Displacement, Log-Law Bounds and von Kàrmàn Constant (see Figure 1 for Definitions)[a]

	d (mm)	κ	Z_R (mm)	Z_R/H	Z_L (mm)	Z_L/H	u_* (m/s)
				Run (I)			
Plane 1	−12.8	0.24	4.1	0.1	17.0	0.4	0.029
Plane 2	−11.4	0.31	2.7	0.1	19.0	0.5	0.028
Plane 3	−9.8	0.25	13.3	0.3	20.3	0.5	0.025
				Run (II)			
Plane 1	−18.0	0.24	9.4	0.2	30.4	0.6	0.035
Plane 2	−17.3	0.21	12.3	0.2	35.2	0.7	0.034
Plane 3	−17.4	0.20	9.0	0.2	34.9	0.7	0.031
				Run (III)			
Plane 1	−14.1	0.26	4.3	0.1	32.6	0.5	0.040
Plane 2	−14.0	0.27	11.4	0.2	34.8	0.6	0.040
Plane 3	−12.1	0.27	5.5	0.1	32.2	0.5	0.041

[a]The shear velocity is obtained by the extrapolation of the Reynolds stress using the PIV data from the individual PIV planes.

and Z_R which are upper and lower bounds of the logarithmic layer; see Figure 1). In the present study, this method was applied to each measurement plane and the summary is given in Table 5. As an example, estimation of d and κ from equations (2) and (3) for two different planes are shown in Figure 11. Table 5 shows that differences in estimates of d, κ, and the log-law bounds in different planes are notable. Moreover, it has to be highlighted that while detection of the log-law region is fairly clear in some planes (e.g., Figures 11a and 11b), it is not so in other planes. For instance, in Figures 11c and 11d a linear behavior for $(d\langle \bar{u}\rangle/dz)^{-1}$ and a constant κ value region are hard to detect. In what follows, we will refer to the log-law fits only the data from plane 2, which is the measurement plane located in the center of the channel. In previous studies, it has been observed that the von Kàrmàn constant may depend on the flow submergence, assuming values lower than 0.41 [*Koll*, 2006; *Gaudio et al.*, 2010]. A potential effect of the relative
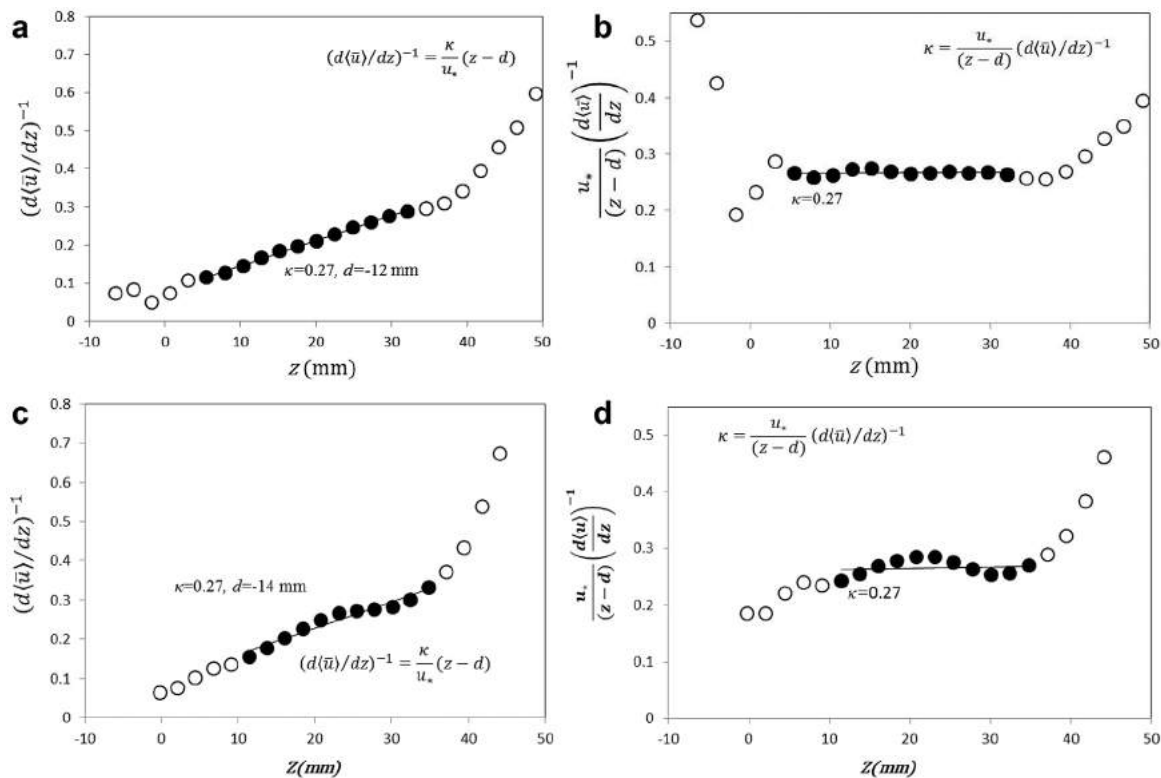

Figure 11. Examples of κ and d evaluation for two different Runs: (a) estimation of κ and d from equation (2), plane 3, Run III; (b) estimation of κ from equation (3), plane 3, Run III; (c) estimation of κ and d from equation (2), plane 2, Run III; (d) estimation of κ from equation (3), plane 2, Run III; circle—experimental data for the whole depth; solid circle—experimental data for the estimated log-law region.
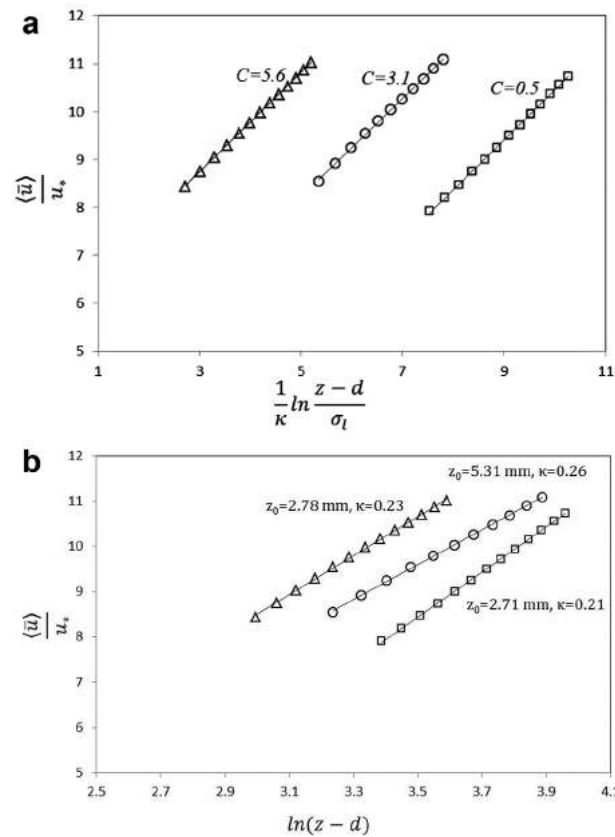
Figure 12. Results of applying the logarithmic velocity approximation in plane 2 (middle of the channel): (a) a log-law form with constant C; (b) a log-law form with hydrodynamic roughness length z_o and κ estimated from equation (1); triangle—Run I; square—Run II; and circle—Run III.

submergence on the zero-plane displacement has not been addressed yet. In fact, it is not yet clear whether the zero-plane displacement is only a function of bed geometry and/or turbulent energy [*Nikora et al.*, 2002] or if it also changes with flow submergence. The present study suggests that the zero-plane displacement may increase with increase of relative submergence, probably reflecting the associated increase in the turbulent energy and prevailing scale, as suggested in *Nikora et al.* [2002]. This matter needs to be better clarified in future studies.

Results of applying equation (1) to the data from plane 2 are shown in Figure 12 for all three runs, including values of the additive constant and hydrodynamic roughness length (note that the von Kàrmàn constant in Figure 12b is estimated using equation (1) instead of equation (2)). These results show that in our experiments not only the von Kàrmàn constant and zero-plane displacement change with relative submergence but also the additive constant and roughness length scale in equation (1).

Spatially averaged turbulent intensities $\langle \sigma_i^2 \rangle^{1/2}/u_*$ for all three runs are reported in Figure 13, together with best-fit expo-
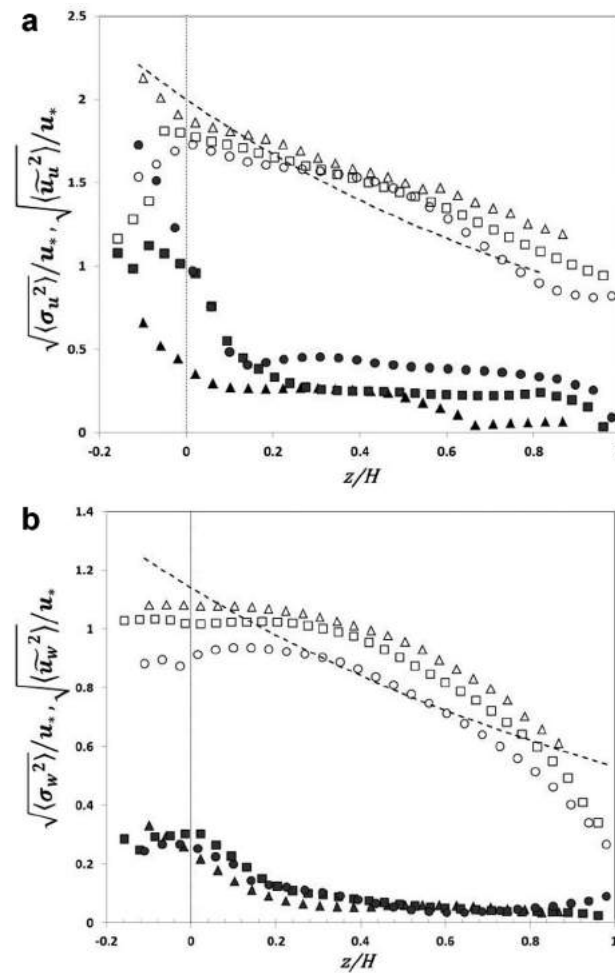
nential curves proposed by *Manes et al.* [2007]. Figure 13a shows that in the central part of the flow, the profiles of $\langle \sigma_u^2 \rangle^{1/2}/u_*$ are similar and almost coincide. In the near-water-surface layer and near-bed region ($z/H < 2.5\sigma_l/H$), however, some small differences are notable (note that $2.5\sigma_l/H =0.38$, 0.29, and 0.25 in Runs I, II, and III, respectively). In particular, $\langle \sigma_u^2 \rangle^{1/2}/u_*$ tends to decrease with increase in the roughness Reynolds number $\Delta^+ =u_*\sigma_l/\nu$, which is associated with increasing relative submergence. This finding is in agreement with the results of *Grass* [1971], *Bayazit* [1976], *Nezu and Nakagawa* [1993], and *Wang et al.* [1993]. On the other hand, *Manes et al.* [2007] did not find significant dependence of $\langle \sigma_u^2 \rangle^{1/2}/u_*$ on the relative submergence, despite using a similar procedure for estimating $\langle \sigma_u^2 \rangle^{1/2}/u_*$.

As for the vertical relative turbulence intensity $\langle \sigma_w^2 \rangle^{1/2}/u_*$ (Figure 13b), its profiles are clearly separated over the whole flow depth, demonstrating higher turbulence intensity for lower flow submergence. This observation also differs from *Manes et al.* [2007] who found no effects of relative submergence on $\langle \sigma_w^2 \rangle^{1/2}/u_*$. Furthermore, our data also differ from that reported by *Grass* [1971] and *Nezu and Nakagawa* [1993], who highlighted a tendency of increase in the vertical turbulence intensity in the near-bed region ($z/H < 0.3$) with increasing $\Delta^+ =u_*\sigma_l/\nu$. This discrepancy suggests that in our data set the turbulence structure depends on the flow submergence stronger than on $\Delta^+ =u_*\sigma_l/\nu$. The unambiguous separation of these two effects for conditions of our experiments is not possible.

The analysis of the form-induced intensities $\langle \tilde{u}_i^2 \rangle^{1/2}/u_*$ shows that despite $\langle \tilde{u}_i^2 \rangle^{1/2}/u_*$ increases near the gravel particle crests, no sharp peaks for $\langle \tilde{u}_i^2 \rangle^{1/2}/u_*$ are visible (Figure 13a and 13b). Although the trends of $\langle \tilde{u}_i^2 \rangle^{1/2}/u_*$ are in agreement with observations of *Aberle et al.* [2008], they somewhat differ from findings of *Manes et al.* [2007] and *Dey and Das* [2012] who revealed fairly sharp peaks of $\langle \tilde{u}_i^2 \rangle^{1/2}/u_*$ at the roughness crests. The form-induced intensity $\langle \tilde{u}_w^2 \rangle^{1/2}/u_*$ assumes values at the gravel crests ranging between 0.2 and 0.3, similar to those obtained by *Manes et al.* [2007] and by *Dey and Das* [2012]. The maximum measured values of $\langle \tilde{u}_u^2 \rangle^{1/2}/u_*$ in the roughness layer range between 0.7 and 1.7, being less than half the maximum

Figure 13. Vertical profiles of spatially averaged turbulence intensity (open symbols) and form-induced intensities (filled symbols): (a) streamwise components $\langle\sigma_u^2\rangle^{1/2}/u_*$ and $\langle\tilde{u}_u^2\rangle^{1/2}/u_*$; (b) vertical components $\langle\sigma_w^2\rangle^{1/2}/u_*$ and $\langle\tilde{u}_w^2\rangle^{1/2}/u_*$; triangle—Run I; square—Run II; and circle—Run III.

values measured in the same region by *Manes et al.* [2007], although very similar to values obtained by *Dey and Das* [2012]. Considering $\langle\tilde{u}_u^2\rangle^{1/2}/u_*$ in more detail, one can also note some increase in its values with relative submergence, especially in the interfacial-sublayer. However, this observation should be treated as indicative only due to potentially high uncertainties in the estimates of $\langle\tilde{u}_i^2\rangle^{1/2}/u_*$ [*Cooper and Tait*, 2010; *Cooper et al.*, 2013].

5. Discussion

In the present study, the measurements of the three velocity components in the near-bed horizontal plane have been combined with two-component velocity measurements in three streamwise vertical planes. This combination provided an opportunity to analyze in detail the characteristics of the flow field at intermediate flow submergence, with particular attention to the near-bed region. Moreover, the conditions of the reported measurements (such as the ratio of vector spacing to the prevailing bed materials size, measurement frequency, flow aspect ratio, and a range of relative submergence) are distinctly different from those reported in the literature [e.g. by *Manes et al.*, 2007; *Cooper and Tait*, 2008; *Hardy et al.*, 2009], allowing us to depict the properties of the flow field at a higher degree of detail.

In the near-bed region, two features of the velocity field have been revealed: (i) streamwise strips of low and high momentum that alternate across the flow and scale with water depth, and (ii) particle-scale patches of flow heterogeneity induced by large bed particles protruding above the mean bed level. The three-component velocity measurements in the near-bed horizontal plane show that the spacing of the streamwise strips is within 1.2–1.6 water depths. High-velocity strips correspond to the areas of downward fluid motion (negative w velocity) while low-velocity strips are associated with upward fluid motion. Furthermore, the sign of the spanwise velocities changes in the middle of the high and low velocity strips. The second-order velocity moments exhibit the similar pattern of longitudinal strips. The two-component velocity data from three vertical planes are consistent with the presence of the strip structure that seems to occupy nearly the whole flow depth. In their combination, the highlighted features lead us to conclude that the "strip" structure in the mean velocity field and second-order moments is a reflection of helical secondary currents. This depth-scale strip structure is superimposed with near-bed patches of flow heterogeneity generated by flow-bed interactions at a bed pebble scale.

The origin of secondary currents in straight uniform open-channel flows can be explained using the x-component of the vorticity equation, which shows that secondary currents are formed when turbulence is anisotropic and flow is spatially heterogeneous [*Einstein and Li*, 1958; *Nezu and Nakagawa*, 1993]. *Nezu and Nakagawa* [1993] stated that the secondary currents are particularly strong near the sidewalls ($y/H \leq 2.5$). However, our measurements show that in a gravel-bed open-channel flow, the secondary currents can be

present even in a region far from sidewalls ($y/H > 2.5$), and may even extend toward the center of the channel. Similar findings have been earlier discussed in the literature [*Nikora et al.*, 1998b; *Rodríguez and García*, 2008; *Albayrak and Lemmin*, 2011]. In particular, *Rodríguez and García* [2008] reported the presence of secondary currents in the central part of flows that had the aspect ratio of 6.3 and 8.5, i.e., close to those in our experiments. On the other hand, the measurements of *Albayrak and Lemmin* [2011] in a very wide open-channel flow ($B=2.45$m) with very high aspect ratio (B/H up to 20) revealed that while secondary currents are well visible even for $y/H > 2.5$, no well-defined secondary current cell can be seen in the central zone. The authors of both papers suggest that the origin of the secondary currents in their studies relates to the difference in roughness between the bed and sidewalls. In the present study, the velocity contour maps in Run III (Figures 6c, 6f, and 6i) show that low and high-momentum "strips" tend to bend around large bed protrusions, which is not as profound in other two runs. This observation may relate to an idea that the secondary flows are induced by bed roughness spatial heterogeneity as suggested by *Barros and Christensen* [2014]. For our case, however, it is difficult to rationally justify that the interference of wakes, induced by randomly placed gravel particles, generates larger-scale and quasi-regularly spaced "strips" of low and high-momentum. Nevertheless, there is experimental evidence that an increase in the roughness difference between bed and side walls seems to enhance secondary currents [*Rodríguez and García*, 2008]. This earlier finding can be supplemented with present results for flow type II showing that the strip structure just above the roughness tops is more evident at lower relative submergence, for which the aspect ratio is higher and equivalent bed roughness is smaller (see Table 1). This seemingly counterintuitive effect can be explained by the fact that the position of the measurement plane was fixed, meaning that it becomes "deeper submerged" in the roughness layer with increasing submergence. The smaller relative distance from the bed z_{plane}/H for higher submergence flows unavoidably leads to increase of the turbulence level and obscureness of the signatures of the overlying secondary currents. As a result, the particle-scale patchiness in flow properties becomes more profound compared to the high-momentum and low-momentum strips that diminish close to the roughness tops. Linking the low-momentum and high-momentum strips to secondary currents in follow-up studies, it is worth exploring a potential connection to coherent superstructures reported recently for pipe and boundary layer flows [*Marusic et al.*, 2010]. In the context of sediment transport, the longitudinal strips of low and high momentum may be directly related to formation and dynamics of sand ribbons [*Karcz*, 1966]. In rough-bed open-channel flows with mobile sediments, cellular secondary currents and sand ribbons are likely to strongly interact leading to stabilization of both the secondary currents and sand ribbons.

Another potential explanation of the "weakened" signature of the secondary currents in higher submergence flows may relate to the insufficient distance from the flume inlet for their full development. Indeed, the current guidelines for estimation of the flow development distance are typically based on the measurements of mean velocity distributions and, occasionally, also on the turbulence measurements. There is no documented information available, however, that would provide guidance for assessing the distance required for the secondary currents to be fully developed. One would reasonably expect that this distance should increase with the flow depth. Thus, it is possible that in relation to secondary currents our higher submergence flows were less developed compared to low-submergence flows (similar effect could occur in *Cooper and Tait* [2010] and *Cooper et al.* [2013] experiments). The potential effect of not fully-developed secondary currents could lead to the results as obtained in our study. The issue outlined above highlights an important omission in the current hydraulic literature related to the assessment of the distance required for secondary currents to be fully developed. A focused study of this matter could also advance the fundamental knowledge on the origin of secondary currents and their maintenance.

The small ratio of the vector spacing to the size of prevailing bed particles in our experiments provided the possibility to detect the disturbances of near-bed flow induced by bed topography, which superimpose and interact with the depth-scale strip structure induced by secondary currents. The horizontal plane data in Figure 6 show that protrusions of gravel crests tend to locally provoke flow diversions in lateral directions. These diversions are quite irregular and seem to be dependent on local orientation and shape of the pebbles that originate them. Furthermore, at the lee region of gravel crests the streamwise velocity tends to decelerate while vertical velocity tends to be downward directed, being typically positive in front of the particles. This pattern seems to contradict to the finding of *Cooper and Tait* [2008] who did not find any correlation between near-bed flow and bed topography. The likely reason of why *Cooper and Tait* [2008] did not

see this pattern could be related to insufficient spatial resolution l_{IA}/D_{50} in their measurement ($l_{IA}/D_{50} \approx 0.5$) compared to the present study ($l_{IA}/D_{50} = 0.05$). Unlike *Cooper and Tait* [2008], *Buffin-Bélanger et al.* [2006] reported that the bed microtopography causes some spatial structure in near-bed flow at a particle scale. They found that maximum and minimum magnitudes of flow velocity modulus occurred at the top of protruding gravel particles and at the lee of large particles, respectively. Complementing this, *McLean and Nikora* [2006] revealed that streamwise and vertical form-induced velocities $\tilde{u}$ and $\tilde{w}$ are correlated with the gravel bed reflecting its main features. As in our study, they found that $\tilde{w}$ usually exhibits maximum (positive) values above the upstream sides of bed particles and minimum (negative) values above their lee sides.

To quantitatively assess the effects of bed topography on the structure of the near-bed flow, we may consider 2-D cross-correlation functions between the time-averaged velocity components, measured in the horizontal plane, and underlying bed elevations, i.e.:

$$R_{\bar{u}_k z_{bed}}(\Delta x, \Delta y) =$$

$$\frac{1}{(N-n)(M-m)} \sum_{i=1}^{N-n} \sum_{j=1}^{M-m} \frac{[\bar{u}_k(x_i, y_j) - \langle \bar{u}_k \rangle][z_{bed}(x_i+n\delta x, y_j+m\delta y) - \langle z_{bed} \rangle]}{\sigma_{\bar{u}_k} \sigma_l} \quad (4)$$

where $R_{\bar{u}_k z_{bed}}(\Delta x, \Delta y)$ is the cross-correlation function; $\Delta x = n\delta x$, $\Delta x = m\delta y$, z_{bed} is a local bed elevation, $\langle z_{bed} \rangle$ is the spatially-averaged bed elevation; σ_l is the standard deviation of bed elevations; $\sigma_{\bar{u}_k}$ is the standard deviation of the kth component of the time-averaged velocity; and N and M are the total numbers of measuring points in the x and y directions, respectively. Before calculation of the 2-D cross-correlation function (equation (4)), a 2-D linear interpolation is applied to the bed elevation measurements to obtain elevations at the same locations for which PIV velocity data are computed.

The obtained 2-D cross-correlation functions are shown in Figure 14. The cross correlograms of the streamwise velocity and bed elevations ($R_{\bar{u} z_{bed}}(\Delta x, \Delta y)$, Figures 14a–14c) have lower absolute maximum values (in all three runs: $|R_{\bar{u} z_{bed}}|_{MAX} \approx 0.3$) compared to the cross-correlograms for the spanwise velocity ($|R_{\bar{v} z_{bed}}|_{MAX} \approx 0.5$; Figures 14d–14f) and vertical velocity ($|R_{\bar{w} z_{bed}}|_{MAX} \approx 0.4$; Figures 14g–14i). Clearly, among three different velocity components, the spanwise and vertical velocities are more strongly affected by bed topography and thus deserve to be considered in more detail. The cross correlograms for the spanwise velocity component show a fairly regular pattern (Figures 14d–14f) that includes positive "hills" in the second and forth quadrants and negative "depressions" in the first and third quadrants. This pattern reflects diverging water motions upstream of the particles and converging water motions at their lee sides. The noted cross-correlogram features are evident for all three runs, although their positions slightly change with relative submergence. The cross correlograms for the vertical velocity (Figures 14g–14i) demonstrate a clear hill at $\Delta y/D_{50} \approx -0.25 \sim 1.00$, which is consistent with upward fluid motion immediately upstream side of gravel particle crests. Downstream of the crests, at $\Delta y/D_{50} \approx -0.25 \sim 1.00$, a negative peak is noticeable, reflecting downflow fluid motion at lee sides of gravel particles. It has to be pointed out that with increasing relative submergence, a progressive decrease of the absolute values of both positive and negative correlation peaks takes place highlighting the submergence effects in the near-bed region.

The analysis of the double-averaged characteristics shows that the normalized streamwise turbulence intensity reveals no significant dependence on the relative submergence although the normalized vertical intensity reduces over the whole flow depth with increasing submergence. Profiles of the normalized vertical form-induced intensity remain approximately the same with increase of the relative submergence, while streamwise form-induced intensity tends to increase in the roughness layer. Although profiles of the normalized vertical form-induced intensity observed in previous studies are also invariable with relative submergence, its effect on the streamwise intensity in the present study is different from what has been previously reported [*Manes et al.*, 2007; *Cooper et al.*, 2013]. *Cooper et al.* [2013] found that the normalized streamwise form-induced intensity is higher at lower submergence, while it remains approximately constant in *Manes et al.* [2007].

The highlighted differences only in part can be explained by the different characteristics of bed topography such as the thickness of the gravel layer or the size and shape of roughness elements. Indeed, one has to bear in mind that the estimates of the double-averaged quantities are sensitive to both the minimum required sample for spatial averaging and density of measurements [*Cooper and Tait*, 2010]. In our study,
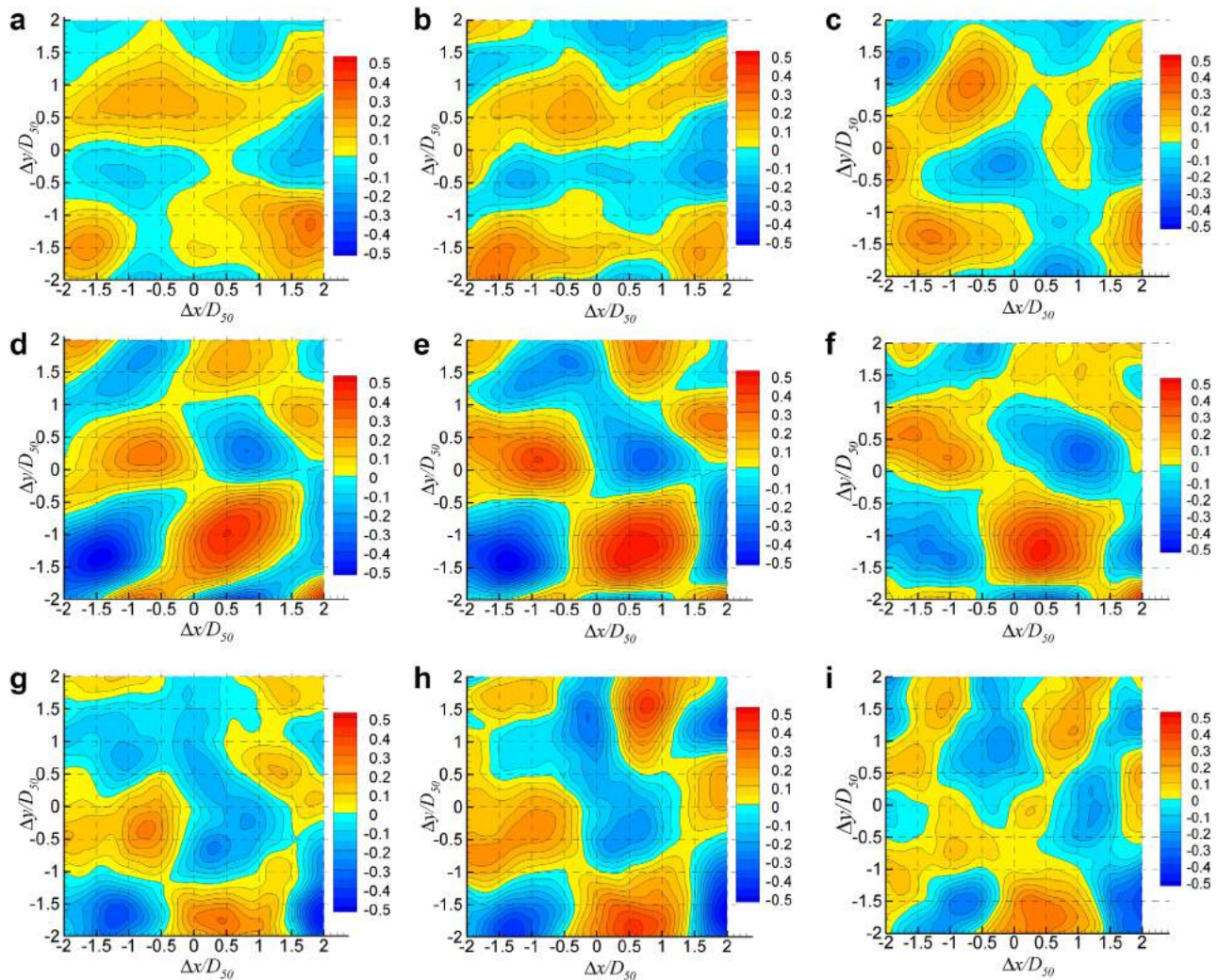
Figure 14. Cross correlogram for near-bed velocity components and bed topography: (a) $R_{\bar{u}z_{bed}}$ for Run I; (b) $R_{\bar{u}z_{bed}}$ for Run II; (c) $R_{\bar{u}z_{bed}}$ for Run III; (d) $R_{\bar{v}z_{bed}}$ for Run I; (e) $R_{\bar{v}z_{bed}}$ for Run II; (f) $R_{\bar{v}z_{bed}}$ for Run III; (g) $R_{\bar{w}z_{bed}}$ for Run I; (h) $R_{\bar{w}z_{bed}}$ for Run II; and (i) $R_{\bar{w}z_{bed}}$ for Run III.

vertical profiles of the double-averaged quantities are obtained using only three vertical planes, which were well separated spatially. To quantify the potential sampling errors for double-averaged quantities obtained from the vertical-plane measurements, we used our PIV data from the horizontal-plane measurements near gravel crests as "true" values. In other words, we compared "well-averaged" quantities at $z/H \approx 0.0$ from the horizontal plane with the corresponding quantities from the vertical planes. Table 6 shows error examples for $\langle \sigma_u^2 \rangle^{1/2}/u_*$ and $\langle \sigma_w^2 \rangle^{1/2}/u_*$. The differences of $\langle \sigma_u^2 \rangle^{1/2}/u_*$ and $\langle \sigma_w^2 \rangle^{1/2}/u_*$ in the horizontal and vertical planes are smaller than 0.2 and 0.4, respectively. Although the observed errors are not significant, they are not small enough to confidently interpret the differences of our results from those previously reported and highlighted above [*Manes et al.*, 2007;

Table 6. Spatially Averaged Turbulent Intensities in the Horizontal Plane and Their Comparison With Corresponding Values in the Vertical Plane

	Run I	Run II	Run III
$\left(\langle \sigma_u^2 \rangle^{1/2}/u_*\right)_{Horizontal}$	1.7	1.8	1.6
$\left\lvert\left(\langle \sigma_u^2 \rangle^{1/2}\right)_{Vertical} - \left(\langle \sigma_u^2 \rangle^{1/2}\right)_{Horizontal}\right\rvert / u_*$	0.2	0.05	0.2
$\left(\langle \sigma_u^2 \rangle^{1/2}/u_*\right)_{Vertical}$	1.5	1.4	1.1
$\left\lvert\left(\langle \sigma_w^2 \rangle^{1/2}\right)_{Vertical} - \left(\langle \sigma_w^2 \rangle^{1/2}\right)_{Horizontal}\right\rvert / u_*$	0.4	0.4	0.2

Cooper et al., 2013]. More detailed measurements are necessary to better determine dependence of the form-induced stresses and other double-averaged quantities in gravel-bed flows on the flow submergence.

Exploring the log-law for velocity distribution and its parameters we found that its performance is not equally satisfactory when applied to different regions across the flow. At different transverse locations, in the regions where it seemingly applies well, the data suggest that the zero-plane displacement, von Kàrmàn constant, hydrodynamic roughness length, and an additive constant depend on the relative submergence. However, it is not yet clear if the applicability of the log-law for flows of intermediate submergence is legitimate in terms of its conceptual justification and in the presence of secondary currents. The data indicate that the log-law may apply for double-averaged quantities, as suggested in *Nikora et al.* [2001], but more work is required to back up this claim for flows of type II.

6. Conclusions

The structure of gravel-bed turbulent flow at intermediate submergence (flow type II) was studied, with particular attention to the near-bed region. Spatial organization of the velocity field was analyzed in the horizontal plane just above gravel particle crests and in three vertical planes at different transverse locations. The bulk flow properties have been analyzed within the framework of the double-averaging methodology including the performance of the log-law and other known approximations for the flow parameters as well as potential effects of flow submergence. The main finding can be summarized as follows.

The near-bed flow field is affected by both gravel bed protrusions and the presence of secondary currents. Particle-scale patchiness of velocity contour maps in the horizontal plane can be ascribed to gravel bed protrusions while secondary currents induce depth-scale low and high-momentum strips profound in the time-averaged velocity field and second-order moments.

Gravel-bed protrusions divert the flow from the main (longitudinal) direction to sidewalls and vertically. Velocity-bed elevation cross correlations show that the effect of bed topography is stronger for spanwise and vertical velocity components. Cross correlograms for vertical velocity reflect upward water motions at the upstream sides of bed particles and downward water motions at their lee sides. The correlograms for the spanwise velocity component suggest prevailing occurrence of flow divergence in front of bed particles and flow convergence behind the particles.

The transverse spacing of depth-scale low-momentum and high-momentum strips is 1.2–1.6 water depths. The effect of the secondary currents is also notable in the second-order moments, increasing with decrease in flow submergence.

The streamwise turbulence intensity in the near-bed region slightly reduces with increase in the relative submergence. Vertical turbulence intensity exhibits a marked decrease over the whole flow depth when submergence increases. Vertical form-induced intensity is almost independent of relative submergence, supporting previous studies. However, differing from the previous studies, the streamwise form-induced intensity reduces with increase in the relative submergence. This difference can be explained by the differences in gravel-bed characteristics in other studies and also by the uncertainty related to high sensitivity of form-induced stress estimates to the measurement protocol.

The performance of the log-law in flows with intermediate submergence remains unclear as well as its conceptual justification and dependence of its parameters on the flow submergence. However, the data of this study suggest that the log-law may apply when considering proper double-averaged quantities and it is worth exploring this direction further.

References

Aberle, J. (2007), Measurements of armour layer roughness geometry function and porosity, *Acta Geophys.*, *55*, 23–32.
Aberle, J., and V. Nikora (2006), Statistical properties of armored gravel bed surfaces, *Water Resour. Res.*, *42*, W11414, doi:10.1029/2005WR004674.
Aberle, J., K. Koll, and A. Dittrich (2008), Form induced stresses over rough gravel-beds, *Acta Geophys.*, *56*, 584–600.
Albayrak, I., and U. Lemmin (2011), Secondary currents and corresponding surface velocity patterns in a turbulent open-channel flow over a rough bed, *J. Hydraul. Eng.*, *137*, 1318–1334.
Barros, J. M., and K. T. Christensen (2014), Observations of turbulent secondary flows in a rough-wall boundary layer, *J. Fluid Mech.*, *748*, R1 pp.

Bayazit, M. (1976), Free surface flow in a channel of large relative roughness, *J. Hydraul. Res.*, *14*, 115–126.

Benedict, L., and R. Gould (1996), Towards better uncertainty estimates for turbulence statistics, *Exp. Fluids*, *22*, 129–136.

Braza, M., R. Perrin, and Y. Hoarau (2006), Turbulence properties in the cylinder wake at high Reynolds numbers, *J. Fluids Struct.*, *22*, 757–771.

Buffin-Bélanger, T., and A. Roy (1998), Effects of a pebble cluster on the turbulent structure of a depth-limited flow in a gravel-bed river, *Geomorphology*, *25*, 249–267.

Buffin-Bélanger, T., S. Rice, I. Reid, and J. Lancaster (2006), Spatial heterogeneity of near-bed hydraulics above a patch of river gravel, *Water Resour. Res.*, *42*, W04413, doi:10.1029/2005WR004070.

Coleman, S. E., V. I. Nikora, and J. Aberle (2011), Interpretation of alluvial beds through bed-elevation distribution moments, *Water Resour. Res.*, *47*, W11505, doi:10.1029/2011WR010672.

Cooper, J., and S. Tait (2008), The spatial organization of time-averaged streamwise velocity and its correlation with the surface topography of water-worked gravel beds, *Acta Geophys.*, *56*, 614–641.

Cooper, J., and S. Tait (2010), Spatially representative velocity measurement over water-worked gravel beds, *Water Resour. Res.*, *46*, W11559, doi:10.1029/2009WR008465.

Cooper, J., J. Aberle, K. Koll, and S. Tait (2013), Influence of relative submergence on spatial variance and form-induced stress of gravel-bed flows, *Water Resour. Res.*, *49*, 5765–5777, doi:10.1002/wrcr.20464.

Davis, A., A. Marshak, W. Wiscombe & R. Cahalan (1994), Multifractal characterizations of nonstationarity and intermittency in geophysical fields: Observed, retrieved, or simulated, *J. Geophys. Res.*, *99*, 8055–8072.

Detert, M. (2008), Hydrodynamic processes at the water-sediment interface of stream beds, PhD, Univ. of Karlsruhe, Karlsruhe, Germany.

Detert, M., V. Nikora, and G. H. Jirka (2010), Synoptic velocity and pressure fields at the water–sediment interface of streambeds, *J. Fluid Mech.*, *660*, 55–86.

Dey, S., and R. Das (2012), Gravel-bed hydrodynamics: Double-averaging approach, *J. Hydraul. Eng.*, *138*, 707–725.

Di Florio, D., F. Di Felice, and G. P. Romano (2002), Windowing, re-shaping and re-orientation interrogation windows in particle image velocimetry for the investigation of shear flows, *Meas. Sci. Technol.*, *13*, 953–962.

Dong, S., G. Karniadakis, A. Ekekci, D. Rockwell (2006), A combined direct numerical simulation–particle image velocimetry study of the turbulent near wake, *J. Fluid Mech.*, *569*, 185–207.

Einstein, H., and H. Li (1958), Secondary currents in straight channels, *Trans. AGU 39*, 1085–1088.

Finnigan, J. (2000), Turbulence in plant canopies, *Annu. Rev. Fluid Mech.*, *32*, 519–571.

Flintham, T., and P. Carling (1988), The prediction of mean bed and wall boundary shear in uniform and compositely roughened channels, in *International Conference on River Regime*, edited by W. P. White, pp. 267–287, John Willy, Chichester, U. K.

Folk, R. L., and W. C. Ward (1957), Brazos River bar [Texas]: A study in the significance of grain size parameters, *J. Sediment. Res.*, *27*, 3–26.

Franca, M., R. Ferreira, and U. Lemmin (2008), Parameterization of the logarithmic layer of double-averaged streamwise velocity profiles in gravel-bed river flows, *Adv. Water Resour.*, *31*, 915–925.

Gaudio, R., A. Miglio, and S. Dey (2010), Non-universality of von Kármán's κ in fluvial streams, *J. Hydraul. Res.*, *48*, 658–663.

George, W. (2007), Is there a universal log law for turbulent wall-bounded flows?, *Philos. Trans. R. Soc. A*, *365*, 789–806.

Goring, D. G., V. Nikora, and I. McEwan (1999), Analysis of the texture of gravel beds using 2-D structure functions, in *River, Coastal, and Estuarine Morphodynamics: Proceedings of the IAHR Symposium*, vol. 2, edited by G. Seminara, et al., pp. 111–120, Springer, N. Y.

Grass, A. J. (1971), Structural features of turbulent flow over smooth and rough boundaries, *J. Fluid Mech.*, *50*, 233–255.

Hardy, R., S. Lane, R. Ferguson, and D. Parsons (2007), Emergence of coherent flow structures over a gravel surface: A numerical experiment, *Water Resour. Res.*, *43*, W03422, doi:10.1029/2006WR004936.

Hardy, R., J. Best, S. Lane, and P. Carbonneau (2009), Coherent flow structures in a depth-limited flow over a gravel surface: The role of near-bed turbulence and influence of Reynolds number, *J. Geophys. Res.*, *114*, F01003, doi:10.1029/2007JF000970.

Hardy, R., J. Best, S. Lane, and P. Carbonneau (2010), Coherent flow structures in a depth-limited flow over a gravel surface: The influence of surface roughness, *J. Geophys. Res.*, *115*, F03006, doi:10.1029/2009JF001416.

Hoover, T., and J. Ackerman (2004), Near-bed hydrodynamic measurements above boulders in shallow torrential streams: Implications for stream biota, *J. Environ. Eng. Sci.*, *3*, 365–378.

Jimenez, J. (2004), Turbulent flows over rough walls, *Annu. Rev. Fluid Mech.*, *36*, 173–196.

Karcz, I. (1966), Secondary currents and the configuration of a natural stream bed, *J. Geophys. Res.*, *71*, 3109–3112.

Kinoshita, R. (1967), An analysis of the movement of flood waters by aerial photography concerning characteristics of turbulence and surface flow [In Japanese], *J. Jpn. Soc. Photogr.*, *6*, 1–17.

Koll, K. (2006), Parameterisation of the vertical velocity profile in the wall region over rough surfaces, *Proceeding of International Conference Fluvial Hydraulics, River Flow 2006 Lisbon Portugal 1*, edited by R. M. L. Ferreira, et al., pp. 163–171, Taylor & Francis, London U. K.

Lamarre, H., and A. G. Roy (2005), Reach scale variability of turbulent flow characteristics in a gravel-bed river, *Geomorphology*, *68*, 95–113.

Lavoie, P., G. Avallone, F. Gregorio, G. P. Romano, and R. A. Antonia (2007), Spatial resolution of PIV for the measurement of turbulence, *Exp. Fluids*, *43*, 39–51.

Manes, C., D. Pokrajac, and I. McEwan (2007), Double-averaged open-channel flows with small relative submergence, *J. Hydraul. Eng.*, *133*, 896–904.

Marusic, I., B. McKeon, P. Monkewitz, H. Nagib, A. Smits, and K. Sreenivasan (2010), Wall-bounded turbulent flows at high Reynolds numbers: Recent advances and key issues, *Phys. Fluids*, *22*, 065103.

Mayes, C., H. Schlichting, E. Krause, H. J. Oertel, and K. Gersten, (2003), *Boundary-Layer Theory*, Springer, Berlin.

McLean, S., and V. Nikora (2006), Characteristics of turbulent unidirectional flow over rough beds: Double-averaging perspective with particular focus on sand dunes and gravel beds, *Water Resour. Res.*, *42*, W10409, doi:10.1029/2005WR004708.

Mignot, E., E. Barthelemy, and D. Hurther (2009), Double-averaging analysis and local flow characterization of near-bed turbulence in gravel-bed channel flows, *J. Fluid Mech.*, *618*, 279–303.

Monin, A., and A. Yaglom, (1971), *Statistical Fluid Mechanics, vol 1: Mechanics of Turbulence*, MIT Press, Cambridge, Mass.

Nezu, I., and H. Nakagawa, (1993), *Turbulence in Open-Channel Flows*, A. A. Balkema, Rotterdam, Netherlands.

Nikora, V. (2008), Hydrodynamics of gravel-bed rivers: Scale issues, in *Gravel Bed Rivers VI: From Process Understanding to River Restoration*, edited by H. Habersack, H. Piégay, and M. Rinaldi, Elsevier, Amsterdam, Netherlands.

Nikora, V., D. Goring, and B. Biggs (1998a), On gravel-bed roughness characterization, *Water Resour. Res.*, *34*, 517–527.

Nikora, V., and J. Walsh (2004), Water-worked gravel surfaces: High-order structure functions at the particle scale, *Water Resour. Res.*, *40*, W12601, doi:10.1029/2004WR003346.

Nikora, V., D. Goring, and B. Biggs (1998b), Silverstream eco-hydraulics flume: Hydraulic design and tests, *N. Z. J. Mar. Freshwater Res.*, *32*, 607–620.

Nikora, V., D. Goring, I. McEwan, and G. Griffiths (2001), Spatially averaged open-channel flow over rough bed, *J. Hydraul. Eng.*, *127*, 123–133.

Nikora, V., K. Koll, S. McLean, A. Dittrich, and J. Aberle (2002), Zero-plane displacement for rough-bed open-channel flows, in *Proceedings of the International Conference on Fluvial Hydraulics River Flow 2002*, pp. 83–92, Louvain-la-Neuve, Belgium, Balkema, Lisse, Netherlands, September 4–6, 2002.

Nikora, V., I. McEwan, S. McLean, S. Coleman, D. Pokrajac, and R. Walters (2007a), Double-averaging concept for rough-bed open-channel and overland flows: Theoretical background, *J. Hydraul. Eng.*, *133*, 873–883.

Nikora, V., S. McLean, S. Coleman, D. Pokrajac, I. McEwan, L. Campbell, J. Aberle, D. Clunie, and K. Koll (2007b), Double-averaging concept for rough-bed open-channel and overland flows: Applications, *J. Hydraul. Eng.*, *133*, 884–895.

Pokrajac, D., J. J. Finnigan, C. Manes, I. McEwan, and V. Nikora (2006), On the definition of the shear velocity in rough bed open channel flows, *Proceeding of International Conference Fluvial Hydraulics, River Flow 2006 Lisbon Portugal 1*, edited by R. M. L. Ferreira, et al., pp. 163–171, Taylor & Francis, London U. K.

Prasad, A. K., R. J. Adrian, C. C. Landreth, and P. W. Offutt (1992), Effect of resolution on the speed and accuracy of particle image velocimetry interrogation, *Exp. Fluids*, *13*, 105–116.

Raupach, M. R., R. A. Antonia, and S. Rajagopalan (1991), Rough-wall turbulent boundary layers, *Appl. Mech. Rev.*, *44*, 1–25.

Robert, A. (1991), Fractal properties of simulated bed profiles in coarse-grained channels, *Math. Geol.*, *23*, 367–382.

Rodríguez, J. F., and M. H. García (2008), Laboratory measurements of 3-D flow patterns and turbulence in straight open channel with rough bed, *J. Hydraul. Res.*, *46*, 454–465.

Scarano, F. (2002), Iterative image deformation methods in PIV, *Meas. Sci. Technol.*, *13*, R1–R19.

Selley, R. C. (2000), *Applied Sedimentology*, Elsevier Sci., San Diego.

Smits, A. J., B. J. McKeon, and I. Marusic (2011), High–Reynolds number wall turbulence, *Annu. Rev. Fluid Mech.*, *43*, 353–375.

Soloff, S. M., R. J. Adrian, and Z.-C. Liu (1997), Distortion compensation for generalized stereoscopic particle image velocimetry, *Meas. Sci. Technol.*, *8*, 1441–1454.

Wang, J., Z. Dong, C. Chen, and Z. Xia (1993), The effects of bed roughness on the distribution of turbulent intensities in open-channel flow, *J. Hydraul. Res.*, *31*, 89–98.

Weitbrecht, V., D. G. Seol, E. Negretti, M. Detert, G. Kühn, and G. Jirka (2011), PIV measurements in environmental flows: Recent experiences at the Institute for Hydromechanics in Karlsruhe, *J. Hydro-environ. Res.*, *5*, 231–245.

Westerweel, J., and F. Scarano (2005), Universal outlier detection for PIV data, *Exp. Fluids*, *39*, 1096–1100.